RESEARCH ARTICLE | SEPTEMBER 06 2023

Observations of plasma waves generated by charged space objects

Special Collection: Papers from the 64th Annual Meeting of the APS Division of Plasma Physics

Paul A. Bernhardt ; Lauchie Scott ; Andrew Howarth ; George J. Morales

Phys. Plasmas 30, 092106 (2023)
https://doi.org/10.1063/5.0155454

Observations of plasma waves generated by charged space objects

Cite as: Phys. Plasmas **30**, 092106 (2023); doi: 10.1063/5.0155454
Submitted: 20 April 2023 · Accepted: 15 August 2023 ·
Published Online: 6 September 2023

Paul A. Bernhardt,[1,a),b)] Lauchie Scott,[2] Andrew Howarth,[3] and George J. Morales[4]

AFFILIATIONS

[1]Geophysical Institute, University of Alaska, Fairbanks, Alaska 99775, USA
[2]DRDC Ottawa Research Centre, Ottawa, Ontario K1A 0Z4, Canada
[3]University of Calgary, Calgary, Alberta T2N 1N4, Canada
[4]Physics Department, University of California, Los Angeles, California 90095, USA

Note: This paper is part of the Special Collection: Papers from the 64th Annual Meeting of the APS Division of Plasma Physics.
Note: Paper YI2 4, Bull. Am. Phys. Soc. **67** (2022).
[a)]Invited speaker.
[b)]**Author to whom correspondence should be addressed:** pabernhardt@alaska.edu

ABSTRACT

A sampling of the environment around inert space objects has determined, which linear and nonlinear waves are created by moving space debris of all sizes. Plasma waves excited by satellites and space debris moving through the Earth's plasma in low earth orbit have been measured with *in situ* electric field sensors on other satellites. These orbit driven plasma waves are of interest for proximity detection of space debris and sources of electrostatic and electromagnetic noise on spacecraft. Satellites and other space objects moving through the near-earth ionosphere between 200 and 1000 km altitude become electrically charged by both electron collection and photo emission in sunlight. These hypersonic, charged objects can excite a wide range of plasma waves. Measurements with the Radio Receiver Instrument (RRI) on the Swarm-E satellite have shown that electromagnetic plasma waves from known objects can be observed out to ranges of tens of kilometers. The amplitude, spectral, and polarization changes of the RRI data are consistent with electromagnetic, compressional Alfvén waves launched by charged space objects traveling across magnetic field lines. In addition, electrostatic lower hybrid waves or nonlinear ion acoustic pinned oscillations may have been self-generated and measured on the Swarm-E satellite. It is proposed that measurements of these waves with local electric field measurements or remote electromagnetic wave scatter may be useful to design systems for the location of orbiting objects. Spatial and temporal details of spacecraft charging are key to understanding the extent of waves associated with the object motion in space plasmas.

I. INTRODUCTION

Plasma wave noise in space is of interest for both space object detection and shielding of sensitive instruments on satellites. First, systems that traditionally detect space debris with satellite and ground sensors use optics and ranging radars but are insensitive to smaller debris. Detection of charged satellites and space debris has been proposed by using nonlinear wave excitations of solitary ion acoustic and magnetosonic waves in low earth orbit (LEO)[1–16] to prevent collisions in space.[17] Second, large space objects have been designed with shielding from external electromagnetic (EM) signals. For instance, polyhedron mesh structures have been proposed to provide protection from external damage by electromagnetic waves.[18] Plasma wave emissions from an object orbiting through an ionized media can enhance the EM noise by penetration though this shielding.

This work supports applications for detection of space debris and unknown satellites with observations the types of waves produced by known objects. Theory, simulations, and laboratory experiments have investigated the possibility of ion acoustic and magnetosonic waves generation in the ionosphere by charged space objects for detection of moving targets. This paper presents the first *in situ* observations of plasma waves from inert space bodies without from active propulsion or artificial electric-field emissions. The amplitude, spectral, and polarization characteristics of the measured electric fields are used to identify the wave types.

The Earth is surrounded by the ionosphere—an atmospheric layer that is 1% ionized with charged particles such as ions and electrons (Fig. 1). All satellites move through this plasma at speeds faster than the speed of sound. Both spacecraft and space debris become electrically charged as they are bombarded by solar light particles and electrons from the plasma environment. Moving charged objects can stimulate a wide range of plasma waves as they travel through the ionosphere and across the Earth's magnetic field lines. The region of plasma oscillations around a small space object may be increased by more than 10 000 from the objects physical size or geometric radar cross section (RSC). Objects normally invisible to radar can be made visible to electromagnetic wave illumination by stimulated scatter from the orbit driven plasma waves.

Plasma wave excitation by space objects can be either steady state or transient. A charged object in an orbit generates a plasma oscillation environment tied to the object. The specifics of the wave dispersion depend on the plasma wave mode. Table I lists the relevant electromagnetic EM and electrostatic modes,[20–22] in a plasma at low and medium frequencies. The nomenclature, frequency range, group velocity, propagation direction, and polarization help identify each wave mode for space observations. These waves are affected by the orientation to the ambient magnetic field and by the plasma density.

The types of waves that can be artificially generated in a magnetized space plasma have been studied using dedicated spacecraft thruster firings in the ionosphere.[23] On 30 July 2009, both Orbital Maneuvering Subsystem (OMS) engines on the Space Shuttle Endeavor were fired for 12 s at a range of 223.8 km from the Vector Electric Field Instrument (VEFI) electric field sensors on the Air Force Research Laboratory (AFRL) C/NOFS satellite. The low frequency, electric field measurements by Vector Electric Field Investigation (VEFI) instrument are illustrated in Fig. 2 where C/NOFS was in orbit at 450 km, 87 km above the orbit of STS-127 flight for the Space Shuttle. The measured waves are consistent with (1) a fast magnetosonic pulse associated with the termination of the OMS burn, (2) intense lower hybrid wave Turbulence from charge-exchange ion beams driving a non-linear lower hybrid-wave instability[23–25] when the exhaust cloud passed over the C/NOFS spacecraft, and (3) weaker ion acoustic waves by the current-driven ion acoustic instability from pickup ions in the exhaust.[26] Figure 2 is an updated plot of the VEFI electric field data with a separation into parallel and perpendicular electric fields relative to the magnetic field direction and a correction of the timing relative to the engine start. As discussed later, the MHD pulse may be a soliton excited by the termination of the OMS engines. The fast N-Wave at 12 s is labeled MHD pulse because the polarization, electric field shape and time delay are consistent with a compressional Alfvén pulse traveling at much greater than the exhaust cloud speed. Not shown in Fig. 2 are higher frequency Precursor Whistler Waves observed in the spectrum of VEFI.[23] These whistlers are excited

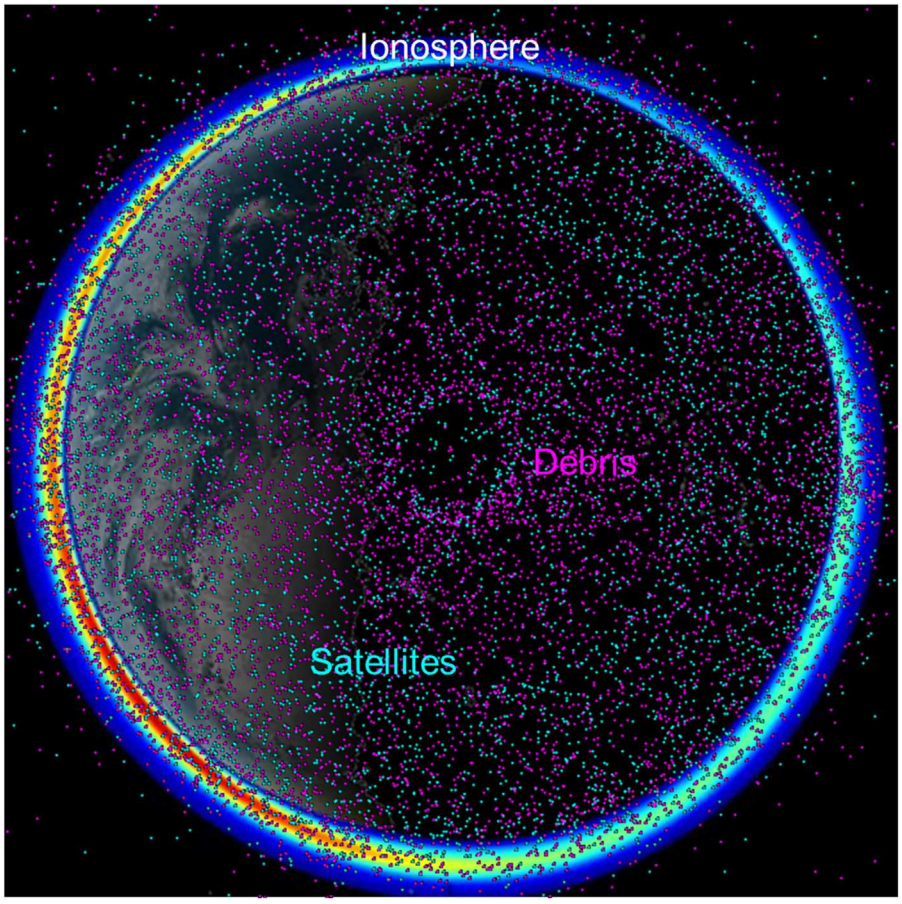

FIG. 1. Polar view of satellites (cyan) and space debris (magenta) superimposed on electron densities in the ionosphere at the limb of the Earth. The ionospheric simulation, shown over the equator, are from the full-physics, 3D model of the ionosphere SAMI3 with the day (left side) and night (right side) variations in electron density.[19] The electron density scale is linear from 0.1 (blue) to 1.0 (green) to 2.0 (red) $\times 10^6$ cm^{-3}. The changes in ionospheric density affect the charging of the space objects. This will influence the plasma wave production in low earth orbit (LEO) as the objects pass through the plasma.

TABLE I. Key features of plasma waves excited by orbiting space objects.

Mode	Alias	Frequency range	Speed	Group direction	Polarization
Fast magnetosonic	Compressional Alfven wave	Low frequency $0 < \omega < \Omega_i$, or ω_{LH}	Fast EM	Isotropic	$\mathbf{E} \cdot \mathbf{B_0} = 0$
Alfven	Shear Alfven wave	Low frequency $0 < \omega < \Omega_i$	Fast EM	Along $\mathbf{B_0}$	$\mathbf{E} \cdot \mathbf{B_0} = 0$
Slow magnetosonic	Magnetized ion acoustic wave	Low frequency $0 < \omega < \Omega_i$, cos θ	Slow ES	Along $\mathbf{B_0}$	$\mathbf{E} \parallel \mathbf{B_0}$ $\mathbf{E} \parallel k$
Whistler	Electron whistler, helicon wave	Medium frequency $\Omega_i, < \omega < \Omega_e$ cos θ	Fast EM	$< 19.5°$ of $\mathbf{B_0}$	$\mathbf{E} \cdot \mathbf{B_0} = 0$
Electrostatic ion cyclotron	First ion cyclotron	Low frequency $\omega^2 = \Omega_i^2$	Zero ES	Isotropic	$\mathbf{E} \cdot \mathbf{B_0} = 0$ $\mathbf{E} \parallel k$
EM ion cyclotron	Second ion cyclotron	Low frequency $\omega^2 = \Omega_i^2 \cos^2\theta$	Slow EM	Along $\mathbf{B_0}$	$\mathbf{E} \cdot \mathbf{B_0} = 0$
Ion acoustic	Unmagnetized ion sound waves	Medium frequency $\Omega_i < \omega < \omega_{pi}$	Slow ES	Isotropic	$\mathbf{E} \parallel \mathbf{B_0}$ $\mathbf{E} \parallel k$
Lower hybrid	Finite-kz lower hybrid waves	Low frequency fixed $\omega_{LH}^2 = \frac{\Omega_i\Omega_e + \Omega_e^2 \cot^2\theta}{1 + \Omega_e^2/\omega_{pe}^2}$	Slow ES	Perpendicular to phase velocity	$\mathbf{E} \cdot \mathbf{B_0} = 0$ $\mathbf{E} \parallel k$

in association with the transients of OMS engine ignition.[23] Late time (>20 s) passage of the exhaust cloud over the electric field sensors yields pickup ions from the hypersonic exhaust that form ion beams and drive instabilities for the electrostatic waves.

Since the pickup ions are moving much faster than the ion thermal speed, the growth rate for the lower hybrid instability[25,27] only depends on the flux of the ion beams and is not affected by the electron temperature relative to the ion temperature. In the region of full charge exchange between ambient O^+ ion and H_2O vapor exhaust, the growth rate for the ion acoustic instability driven by an ion beam current is

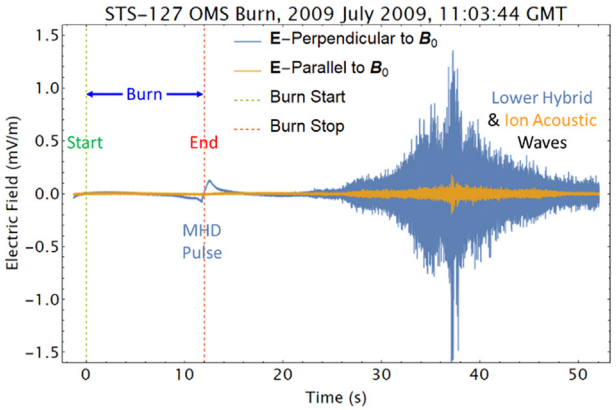

FIG. 2. Plasma wave electric fields obtained with the VEFI instrument on C/NOFS following the 12 s injection of 3×10^{27} molecules of rocket exhaust. These waves have been identified based on frequency, polarization, and time delays for the engine burn 223.8 km from the electric field detectors. Since the pickup ions are moving much faster than the ion thermal speed, electron Landau damping is unimportant for the perpendicular propagating lower hybrid (LH) waves but does attenuate the ion acoustic waves.

$$\gamma_{IA} = \omega_{IA}\sqrt{\frac{\pi}{8}}\left[\left(\frac{m_e}{m_i}\right)^{1/2}\left(\frac{U_0}{c_s} - 1\right) - \left(\frac{T_e}{T_i}\right)^{3/2} exp\left(-\frac{T_e}{2T_i}\right)\right], \quad (1)$$

where U_0 is the ion beam velocity and c_s is the ion acoustic speed. This instability is damped out unless the electron temperature is much larger than the ion temperature. The ion acoustic waves are weak in Fig. 2 because of Landau damping in (1). The identification of the plasma wave modes was based on the frequencies and electric field polarization according to the criteria listed in Table I. In addition to the four wave modes of fast magnetosonic, lower hybrid, ion acoustic, and whistler, no other mode listed in Table I has been previously observed.

In situ measurements of plasma waves excited by space objects in low earth orbit (LEO) are presented in Secs. II and III with emphasis on (1) identifying the wave modes and (2) experimental conditions for production of these waves. Section II illustrates the plasma wave oscillations produced on the host satellite that is making the electric field measurements. This is followed by Sec. III on the electric field observations when sensors on a host satellite pass through the plasma wave environment found within 100 km of target satellites. Both of these sets of observations show that compressional Alfvén (i.e., fast magnetosonic) waves and oblique (i.e., finite k_z) lower hybrid waves are generated by charged object motion in space.

Section IV surveys theories that can account for the observations with either constant or time varying charging of the space objects. The generation of plasma waves is affected by both the orbit angle with magnetic field lines and object charging processes. Section IV A describes steady state solutions from an object with a fixed electric charge. The resulting electric field disturbances can be either linear waves spread across the orbit in the wake or nonlinear solitons pinned to an orbiting object. Section IV B examines time variations in plasma waves in the orbit reference frame caused by time variations in the charging of the object. The sudden charging of a spacecraft can launch precursor solitons that travel relative to the charged source. In Sec. V,

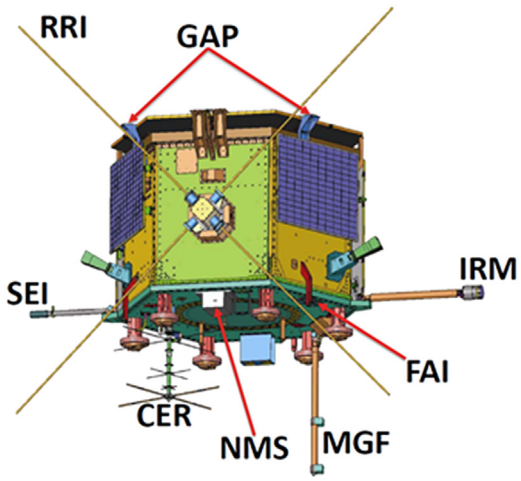

FIG. 3. Swarm-E/e-POP small-satellite instrument payload launched on 29 September 2013. The particle instruments IRM (Imaging Rapid Ion Mass spectrometer), SEI (Suprathermal electron imager), and NMS (Neutral Mass and Velocity spectrometer), the optical camera FAI (Fast auroral imager), wave receivers RRI (E-Field receiver), MGF (Magnetometer), GAP (Differential GPS) and radio beacon CERTO (Radio tomography) provide eight sensors that are ideal for space debris investigations. The Swarm-E/CASSIOPE satellite image is open source from Magellan Aerospace.[28]

the detection of these spacecraft driven plasma waves is discussed in terms *in situ* conjunctions with electric field proximity sensors or scattering of electromagnetic waves from ground HF transmitters. Section VI states that the *in situ* observations of space object electric fields are consistent with compressional Alfvén waves limited in frequency by finite-k_z lower hybrid waves.

II. OBSERVATIONS OF SELF-GENERATED PLASMA WAVES AROUND HOST SATELLITES

Prior to conducting experiments to observe the wave generated by other satellites, measurements were made of plasma wave modes generated by the host satellite itself. The Swarm-E spacecraft (also known as CASSIOPE) was used for these observations (Fig. 3).

Archived data from the RRI (Radio Receiver Instrument) electric field instrument have been analyzed to determine if the orbital motion of Swarm-E satellite body and booms could create plasma emissions. The spacecraft produces a VLF spectral feature called the Spontaneous Plasma Wave Emission (SPWE).[29] Figure 4 illustrates an examples of the SPWE near 15 to 20 kHz for satellite motion oblique to the magnetic field $\mathbf{B}_0$. These waves are observed above the local values of the ion cyclotron and lower hybrid frequencies. The data show frequency shifts, spectral spread, and intensity variations that may be related to changes in the object charging, background plasma density, and orbit direction. For the observed SPWE frequency ranges, the SPWE could be local (a) ion acoustic or (b) off-perpendicular lower hybrid waves.

Pinned ion acoustic solitons in the form of ion acoustic waves have been predicted by nonlinear simulations driven by charged spacecraft motions above the local ion acoustic speed.[1,2,5–7,10,12,13,15,30] The observations of the SPWE previously published by Bernhardt *et al.*[29] and shown Fig. 4 may be the first confirmation of this process by *in situ* measurements of satellite electric fields. Production of nonlinear ion acoustic waves is described in Sec. IV. The intensity and frequency spread of ion acoustic pinned solitons may represent changes in the Swarm-E charging.

Waves produced with frequencies above the local lower hybrid frequency (~7 kHz) are also consistent with the *in situ* observations (Fig. 4) that with an orbit angle of 76° with $\mathbf{B}_0$, change and are polarized perpendicular to the ambient magnetic field direction. According to the properties in Table I, these waves are consistent with lower hybrid (LH) modes that are propagating slightly off perpendicular to the magnetic field line direction.[31] This result is important for showing that cross-magnetic-field satellite motion in space excites finite k_z lower hybrid waves. These waves are sources of noise for host satellites employed to detect plasma waves generated by the motion of target space debris through the ionosphere. It is significant that these local waves only exist for frequencies above the local value of the lower hybrid frequency. The waves detected from other satellites are shown in Sec. III to be below the lower hybrid frequency so self-generated disturbances do not contribute to the receiver noise spectrum.

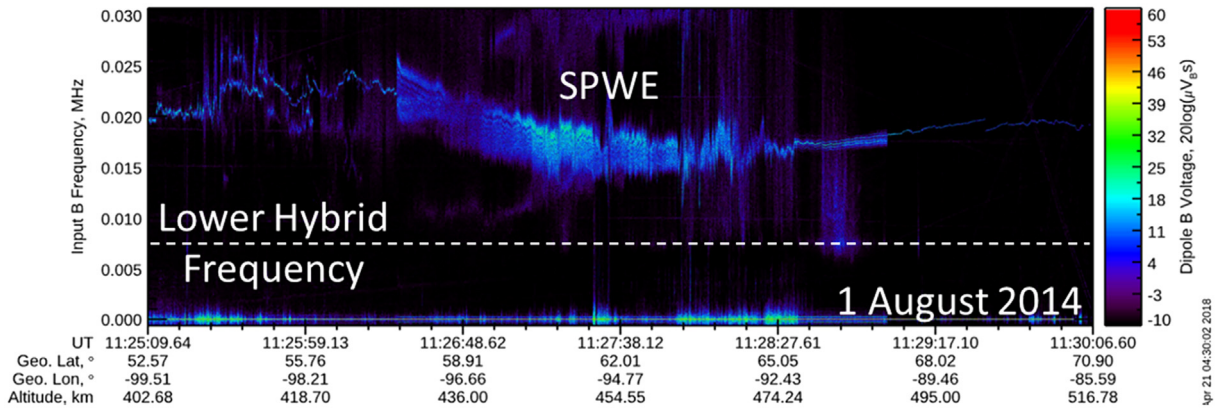

FIG. 4. Spectrogram of the Self-Generated Spontaneous Plasma Wave Emissions (SPWE) on the Swarm-E satellite using the radio receiver instrument RRI. The narrow and wide emissions have frequencies above both the local lower hybrid frequency near 7 kHz and the ion gyro frequency at 50 Hz. The emissions are found when Swarm-E/e-POP moves nearly perpendicular to $\mathbf{B}_0$.

The generation of waves in the lower hybrid frequency range can be caused by density gradients in the near environment of plasma clouds,[32] and dust and space objects.[33] The situation with magnetized electrons and unmagnetized ions is favorable for the excitation of lower hybrid waves by the lower hybrid drift instability (LHDI)[32,34–37] or the electron–ion hybrid mode if there is shear in the cross field electron flow.[38] These waves have been observed with diamagnetic cavities formed by plasma clouds[32] and comets.[34,37,39] Moving space debris in a plasma will charge to a negative potential leading to wake enhancements of both ion and electron densities over the ambient values.[3] The diamagnetic drifts across $\mathbf{B}_0$ that develop due to density changes can drive the LHDI and ion–ion cross field instability to excite lower hybrid waves at the space object.[32,39] These electrostatic wave modes will not propagate much farther than an ion gyroradius (~5 m) from the spacecraft.

Practical detection of plasma waves from space debris using *in situ* proximity sensors would need waves that propagate to a much larger distance than an ion gyro radius but localized waves are important to validate the wave production process at the charged space object. Section III provides a sample of disturbances recorded for target space objects using the RRI electric field sensors at ranges of 1 to 100 km.

III. *IN SITU* OBSERVATIONS OF PLASMA WAVES GENERATED BY TARGET SATELLITE

Motivated by theoretical predictions that charged spacecraft can produce plasma waves,[3] the Canadian Swarm-E satellite was used to measure the plasma wave environment around satellites and space debris. Electric fields of spacecraft-generated waves were obtained as the Swarm-E host-satellite passed close to several targets including satellites and space debris in low earth orbit. Swarm-E has the ideal orbit for LEO satellite encounters with an apogee of 1500 km and a perigee of 325 km. For instance, this orbit passes through the 550 km altitudes of the 2500 Starlink satellites 28 times a day (Fig. 5). These observations are organized into a database according to the distance between host and target, the satellite-target physical size, radar cross section (RCS) of the hard body at a specific frequencies, orbit attitude and velocity, the target motion relative to magnetic field lines, etc., where multiple space objects are scheduled for target objects within 1 km of Swarm-E/e-POP sensors. With the existing download capability for the satellite, 2-min conjunction data are collected up to three and five times a day.

Mission planning, data storage, and downloading were required to collect the electric field measurements. Two to three days prior to data acquisition, DRDC—Ottawa Research Center and UAF compute high precision trajectories of both active satellites and space debris to determine when the Swarm-E satellite would pass through the ion-acoustic Mach cone of the target objects. The data are collected for a 3 to 10-min period centered on the encounter time between Swarm-E and the space object target. The Swarm-E satellite maintains a solar pointing orientation during the observation periods with precise knowledge of satellite position and antenna boom orientation. The minimum conjunction distance will be less than one kilometer. After data are downloaded from Swarm-E, they are stored by the University of Calgary at e-POP Data Archive https://epop-data.phys.ucalgary.ca/. The data are analyzed by the Geophysical Institute at the University of Alaska at Fairbanks to determine the measured frequency spectrum

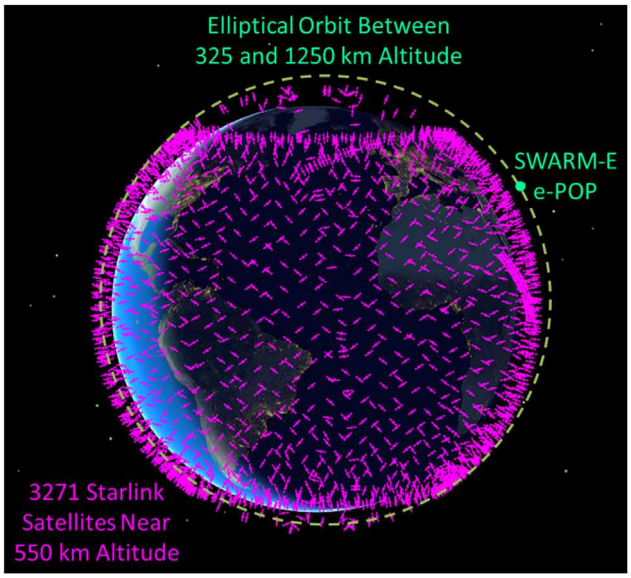

FIG. 5. The 325 × 1100 km elliptical orbit of Swarm-E passes near the trajectories of Starlink and other space objects in low earth orbit for measurements of *in situ* electric fields. Observations of orbit driven waves have been observed in the 10 Hz to 35 kHz range. This figure was produced using the Satellite Orbit Analysis Program (SOAP) Version 15.5.3 from The Aerospace Corporation.

and time series for RRI channels A and B of the RRI electric field boom antennae (Fig. 3).

A schematic of the data collection geometry and sampled electric field data during four successful measurements are illustrated in Fig. 7. The wave disturbance amplitudes for satellites and space debris are collected with electric field sensors on the host satellite that passes less than 50 km from a target. The minimum range to the target is shown for each example. Measurements are made in the F-region of the ionosphere for targets in low earth orbit. The four insets are associated with two Starlink satellites, one small space debris and a large Iridium satellite. None of these objects had thruster operations during the measurement periods. They all show a strong FLASH signature of the satellite amid ambient spikes and lower amplitude noise. The trajectories of the Swarm-E/RRI host sensor and a target space object that cross paths are shown with green and red vectors, respectively. The data insets are time series of the electric fields recorded on the Swarm-E spacecraft from either the A or B channel of the RRI instrument. For the four time-series in Fig. 6, the data are processed with a bandpass filter between 1 and 6 kHz to reduce the background interference noise such as spikes from coherent transmissions by ground VLF transmitters, lightning produced whistlers, and other natural VLF generation processes. The FLASH label is given to each time series indicating a long duration burst of electric fields with a waveform shape and amplitude distinct from the background electric field noise.

The experimental conditions for the four RRI observations in Fig. 6 are provided by Table II. Parameters such as target size, time, position, solar illumination, orbit velocity relative to magnetic field $\mathbf{B}_0$, disturbance region size, and state of the background plasma are indicated to help understand the physical process for FLASH generation. The last three tests have FLASH signatures that occur at the predicted

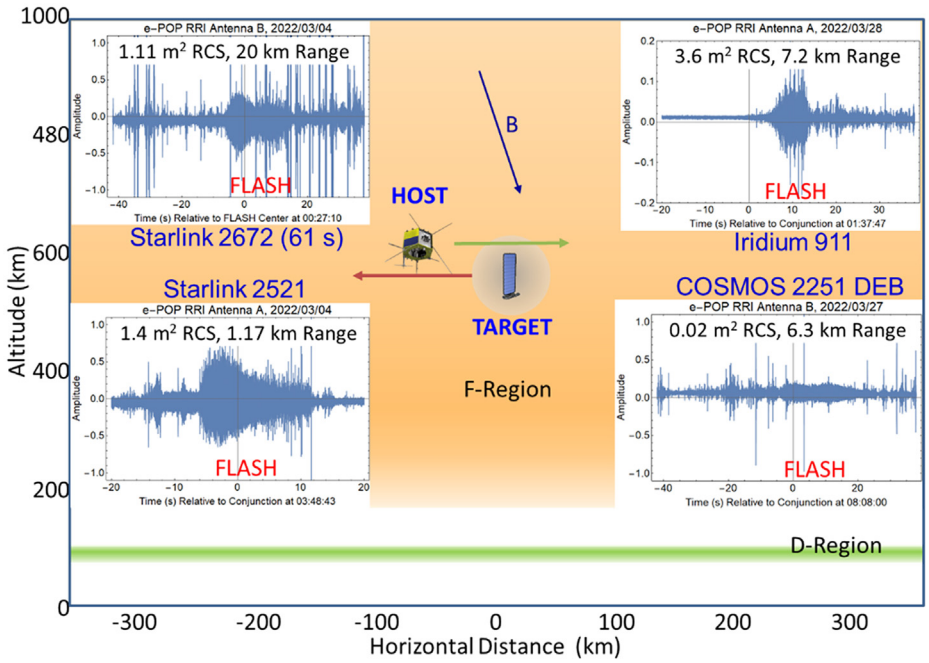

FIG. 6. Measurements of electric fields during *in situ* experiments by the Swarm-E satellite using the Radio Receiver Instrument (RRI). The artificially enhanced plasma waves are labeled as a FLASH.

times of closest approach and have target orbit motion nearly perpendicular to $\mathbf{B}_0$. For all observations, the Alfvén speed is about 1000 times larger than the ion acoustic speed, the space objects are moving around 7.8 km/s which is much smaller than the Alfvén velocity and larger than the ion acoustic speed. All targets are on trajectory line distances less than 1 km from the RRI, but the minimum distance between the target and host ranges from 1 to 20 km. The largest separation was for Test #1 and had (a) the highest error in FLASH observation time relative to predicted conjunction and (b) the longest flash duration. The measured plasma oscillations are fast magnetohydrodynamic (MHD) waves and finite-k_z LH waves that are seen as far as 90 km from the target space object. The four satellite tests demonstrate

TABLE II. Conjunctions of target satellites and space debris with RRI hosted on Swarm-E.

	Test #1	Test #2	Test #3	Test #4
Targets	Starlink 2672	Starlink 2521	COSMOS 2251 DEB	IRIDIUM 911
Date time GMT	4 Mar 22 00:27:15	4 Mar 22 03:48:43	27 Mar 22 08:08:00	28 Mar 22 01:37:47
Altitude (km)	551.5	551.2	76.35	754.6
Latitude (°)	−30.2	−15.8	70.4	−68.5
Longitude (°)	35.9	−26.5	201.2	119.9
Solar illumination	Dark: −37 Elev.	Dark: −56 Elev.	Sunlit: −13 Elev.	Sunlit: 14 Elev.
Orbit inclination (°)	53.06	53.06	74.02	86.45
Time to conjunction (s)	−61	0	5	10
FLASH duration (s)	25	20	20	10
Minimum distance (km)	19.6	1.17	6.3	7.22
Detection range (km)	135	170	50	150
Trajectory separation (m)	106	68	581	604
RCS (m^2)	1.11	1.42	0.02	3.58
Orbit angle to B (°)	56.8	75.8	86.2	89.6
Target speed (km/s)	7.3	7.3	7.4	7.4
Debye length (cm)	1.6	1.8	6.0	4.0
Ion acoustic speed (m/s)	846	714	1216	1281
Alfven speed (Mm/s)	1.4	2.1	3.0	1.3

that localized enhancements in electric field noise show the presence of spacecraft moving though ambient plasma over ranges of 50 to 170 km.

Each of the experimental tests are examined in detail. Figure 7 shows the geometry for Test #2 along with a sample burst of enhanced wave noise. The peak of this enhanced signal is near the point of closest approach between the RRI sensor and Starlink 2521. The burst of plasma-wave noise lasts 18 s and is interpreted as spacecraft-driven turbulence from a mixture of plasma waves. This experiment was designed to have the host sensor pass through a trailing trajectory cone to look for plasma turbulence in the wave of the target. Starlink confirmed that the Krypton ion thruster on the spacecraft was not in operation during or within 90 min of these measurements.

The time series of electric field data is converted into a spectrogram to identify the frequency components of the plasma wave modes. Figure 8 is a spectrogram of the Channel A data shown in Fig. 7. The frequency spectra indicate that primarily fast magnetosonic (compressional Alfvén) waves are generated along with ion cyclotron, lower hybrid, ion sound, and whistler waves around the spacecraft. The horizontal lines between 15 and 30 kHz are VLF signals from ground transmitters. In addition to the frequency range, the electric field polarization perpendicular to $\mathbf{B}_0$ indicates that a compressional Alfvén wave with a lower hybrid cutoff frequency is the dominant mode.

The FLASH burst spectrum for Test #1 shows similar features such as emissions primarily extending from the local ion cyclotron frequency to the local value for the lower hybrid waves (Fig. 9). In addition, there are large extensions above f_{LH} that are probably whistler modes. Natural whistlers are cutoff at the lower hybrid frequency at

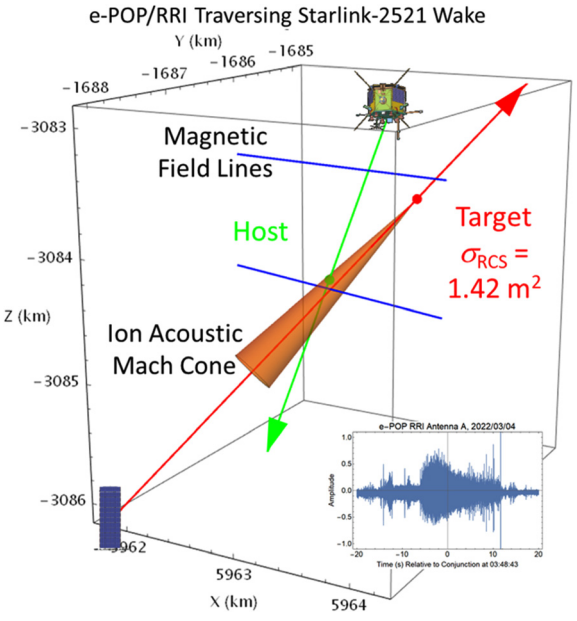

FIG. 7. Trajectories of the Starlink 2521 (red, bottom-left) encounter with RRI sensor (green, top-center) showing an electric field "FLASH" (inset) 20 dB above the background noise level. The orange cone represents a region of either Cherenkov radiation or ion acoustic shock boundary from an electrically charged Starlink satellite.

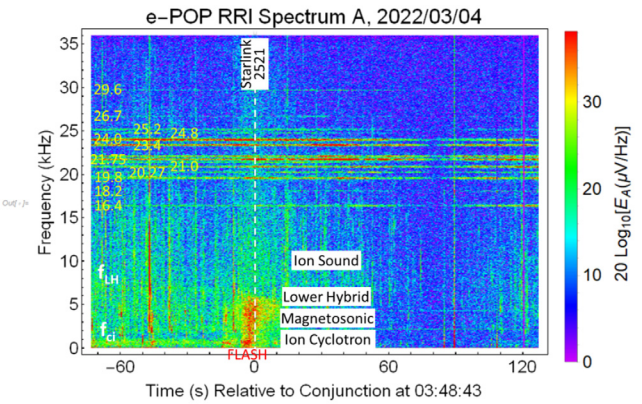

FIG. 8. Conjunction on 4 March 2022 between the Swarm-E host and the Starlink 2521 target satellites showing the FLASH burst spectrum. The bulk of the oscillations are below the lower hybrid frequency at the time of closest approach between the spacecraft.

the limit of propagation with large wave normal angles.[37] The range of Starlink 2672 from the Swarm-E sensor is 450 km at the time of these measurements. This may indicate that charged space objects can generate strong compressional Alfvén waves and weak whistler modes that can be detected hundreds of km from the targets. It also may indicate that the timing of the Starlink 2672 orbit predictions was in error by one minute or that other space objects were responsible for the FLASH in Fig. 8. A search of satellite orbits at the time of Test #1 found that a piece of COSMOS 1408 Debris and a Starlink 1582 were at minimum ranges of 208 and 85 km, respectively, from Swarm-E during the measurement period. Finally, it is noted that the time–frequency distribution of the flash spectrum for the two Starlink targets (Figs. 8 and 9) are similar possibly because (1) both targets are at the same altitude in similar plasmas or (2) both objects have the same physical shape.

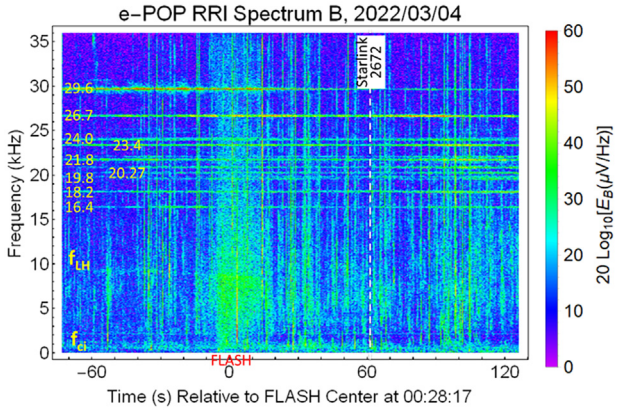

FIG. 9. Successful measurements for the test on 4. March 2022 with Starlink and Swarm-E Satellite detection of wave generation in satellite wakes. The 61 s offset in satellite conjunction predictions may be from orbit ephemeris error or the presence of other satellites at the same orbit altitude in the vicinity of Swarm-E.

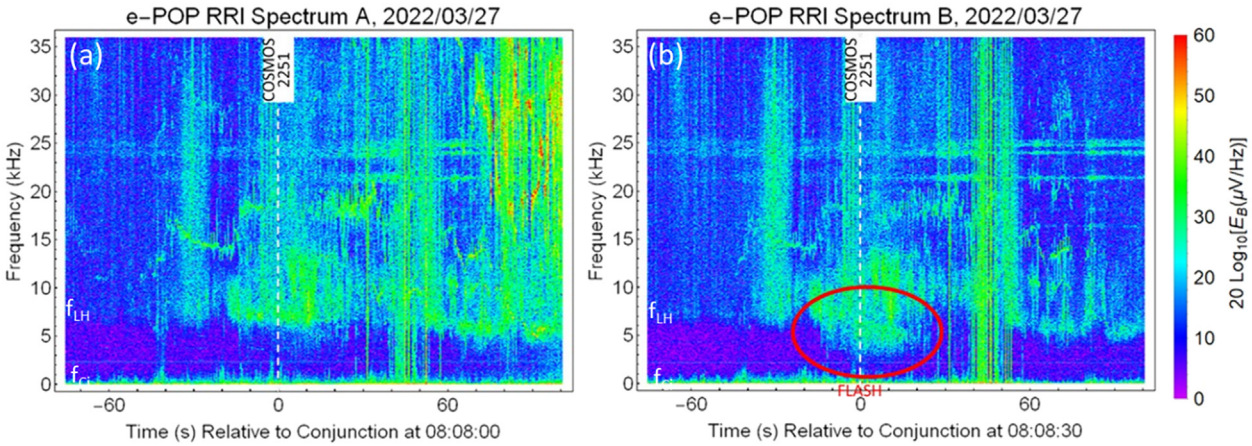

FIG. 10. Normal (a) and unusual (b) observations of the COSMOS-2251 space debris encounter with the Swarm-E RRI electric field showing a FLASH only on the B-Channel (outlined in red). The 20 dB electric field enhancement at the time centered on the encounter (b) is a broad spectrum below the lower hybrid frequency with a 50 s duration and a 100 km disturbance cloud radius. This is interpreted as plasma waves driven by space debris motion across **B** leading to *in situ* radiation of strong fast magnetosonic waves characterized by cross field polarization.

FLASH bursts can be found in only one of the two channels of the RRI. The observations shown in Fig. 10 were made with a small space debris (~10 cm) from the collision of the Russian COSMOS 2251 with the Iridium 33 satellite. The two A and B channels of the RRI show totally different results below the 8 kHz lower hybrid frequency. The plasma waves recorded with antenna A of the RRI do not show any enhanced plasma wave activity below the lower hybrid frequency (Fig. 10, left). Channel B of the RRI, however, shows a strong FLASH extending down in frequency from f_{LH}. This is consistent with electric fields that are polarized perpendicular to the ambient magnetic field such as identified with compressional Alfvén waves. Since there are only two (x–y) dipole antennas with the RRI, the full three-dimensional (3D) polarization cannot be determined. Future satellites used to detect plasma wave signatures of space objects should have three-axis electric field sensors as well as magnetic field sensors.

Care must be taken that plasma wave bursts, attributed to a designated target event, may be of natural origin. The strong FLASH 10 s after transit of Iridium-911 (see Figs. 11 and 12) might be coincident with the passage of the Swarm-E spacecraft across a high latitude boundary associated with the plasmapause. The plasma wave spectrum for this event (Fig. 12) shows waves with extensions down from 15 kHz to below the lower hybrid frequency of 8 kHz.

Using the RRI instrument on Swarm-E, 58 conjunction experiments were conducted with satellites and space debris. A small fraction (~10%) of the observations show coincident FLASH bursts ranging from below ion cyclotron and just above lower hybrid frequencies. Sometimes the FLASH E-field signatures are absent or are masked by geophysical plasma wave interference from lighting driven whistlers, solar substorm hiss and noise, and ground VLF transmitters. The utility of these measurements is determined by what plasma waves are produced by passive space objects, what are the conditions for their production, and validation theoretical models the predict their occurrence. Some of these models are reviewed in Sec. IV. More observation and data downloading time is needed. A three-axis set of dipoles would also improve wave detection and model identification.

The observations illustrated by Figs. 6–12 demonstrate that the three domains of amplitude, frequency, and polarization may be used to identify signals from passive space debris. The FLASH amplitude envelopes in Fig. 6 have strong signatures for the Starlink 2521, 2672, and Iridium 911 space objects. The amplitude envelope in Fig. 8 for the smaller space debris of COSMOS 2251 has an amplitude near the background VLF hiss. This does not mean that the COSMOS 2251 debris, with a smaller physical size, would not be detected by *in situ*

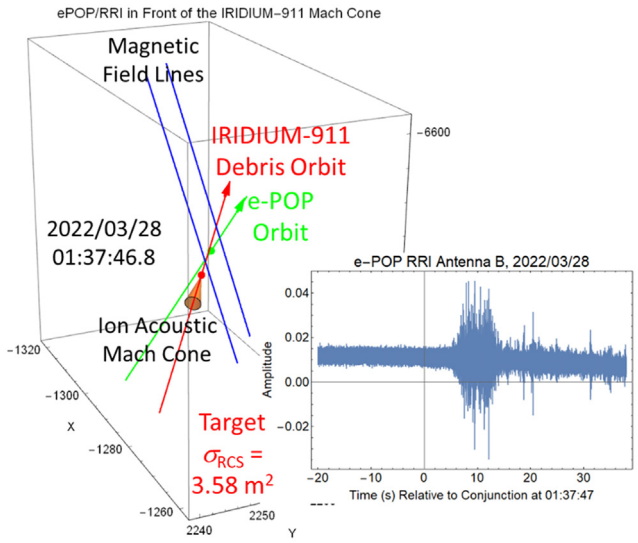

FIG. 11. Conjunction of the Iridium-911 satellite with the RRI sensor in the e-POP sensor suite of Swarm-E. The trajectories are timed so the host sensors pass across the target trajectory in front of the target. Both target and host satellites are moving northward from the southern hemisphere.

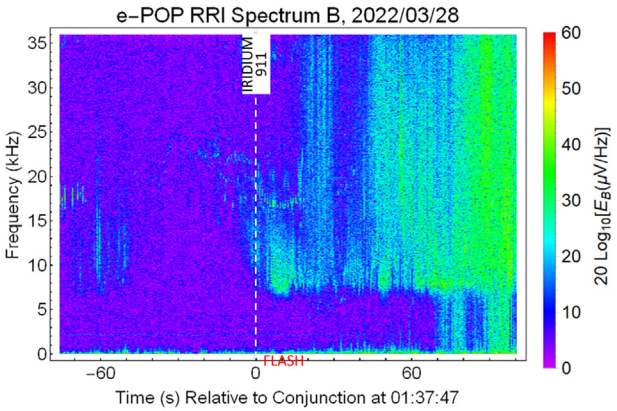

FIG. 12. Test #4 on 28 March 2022 with IRIDIUM 911 and the e-POP/RRI sensor passing near the satellite wake. The FLASH spectrum may be produced by the charged satellite or by passage across a low altitude projection of the plasmapause. Here, the Swarm-E electric field sensor travels northward in the southern hemisphere.

electric field probes but that frequency and polarization domain observations need to be included. The Starlink 2251, 2672, and COSMOS 2251 debris have frequency spectra that have an upper frequency cutoff at the local value of the lower hybrid frequency (Figs. 8–10). The COSMOS 2251 debris signals are polarized perpendicular to the magnetic field with a 20-dB signal to noise ratio (Fig. 10). Finally, the strong Iridium 911 signal starts below, but extends above, the lower hybrid frequency with an 8-dB signal to noise ratio. These observations indicate that unknown space debris could be found with *in situ* proximity sensors. Orbiting three-axis dipole probes could be employed to search for amplitude changes in the time domain, frequency spectrum up to lower hybrid cutoffs, and electric fields polarized normal to the ambient magnetic fields. In addition, the use of three-axis magnetometers or magnetic loops could distinguish the electromagnetic MHD waves from the electrostatic modes.

The temporal variations of the electric field measurements with moving host sensors and moving target objects can be produced by either sensors passing through the steady state spatial environment of a space object or with the influence of time-varying changes of the waves emanating from the charged object. The steady-state environment tied to the frame of the space object is called a pinned disturbance. Propagating electric fields launched away from the frame of the charged object are called a precursor disturbances. Precursor waves can be generated with a temporal transients in the object charging. Both steady state and transient wave sources are considered next.

IV. THEORETICAL INTERPRETATION AND MODELS FOR THE ELECTRIC FIELD OBSERVATIONS

Based on the new observations with the *in situ* techniques of Sec. III, the type of plasma oscillations excited by orbiting space objects can be interpreted by comparison to theory and simulations. The electric field oscillations, **E**, excited by an external current, $\mathbf{J}_{Ext}$, from the motion of a charged spacecraft is described by the following equations:

$$\nabla\times\nabla\times\boldsymbol{E}(\boldsymbol{r},t)+\varepsilon_0\mu_0\frac{\partial^2\boldsymbol{E}(\boldsymbol{r},t)}{\partial t^2}=-\mu_0\frac{\partial}{\partial t}[\boldsymbol{J}_{Ext}(\boldsymbol{r},t)+\boldsymbol{J}(\boldsymbol{r},t)],$$
$$\boldsymbol{J}(\boldsymbol{r},t)=n_0e(\boldsymbol{v}_i-\boldsymbol{v}_e),$$
$$\rho_0\frac{\partial\boldsymbol{v}}{\partial t}=\boldsymbol{J}\times\boldsymbol{B}_0-\nabla p+\rho_0\nu_n(\boldsymbol{v}_n-\boldsymbol{v}),$$
$$\frac{m_e}{n_0e^2}\frac{\partial\boldsymbol{J}}{\partial t}=\boldsymbol{E}+\boldsymbol{v}\times\boldsymbol{B}_0-\frac{m_i}{e}\frac{\partial\boldsymbol{v}}{\partial t}-\frac{\nabla p}{n_0e},\quad \boldsymbol{v}=\frac{\rho_{0i}\boldsymbol{v}_i+\rho_{0e}\boldsymbol{v}_e}{\rho_{0i}+\rho_{0e}},\tag{2}$$
$$\frac{\partial p}{\partial t}=-\frac{n_0c_s^2m_i}{\omega}\nabla\cdot\boldsymbol{v}+\frac{(1-g)c_s^2m_i}{e}\nabla\cdot\boldsymbol{J},$$
$$c_s^2=\frac{\gamma_e\kappa T_e+\gamma_i\kappa T_i}{m_e+m_i},\quad g=\frac{\gamma_iT_i}{\gamma_eT_e+\gamma_iT_i},$$

which are based on Maxwell's equations, ion and electron continuity and momentum equations, and the equation of state.[20–23,40,41] The linear (first order) wave, where the density fluctuations waves are small compared to the background density ρ_0, are extracted from configuration space, **r**, and time, t, to wave number **k** and frequency ω using the Fourier transform kernel $e^{-i(\mathbf{k}\cdot\mathbf{r}-\omega t)}$, yielding the following expression:[22,42]

$$\boldsymbol{k}[\boldsymbol{k}\cdot\tilde{\boldsymbol{E}}(\boldsymbol{k},\omega)]-k^2\tilde{\boldsymbol{E}}(\boldsymbol{k},\omega)+k_0^2\boldsymbol{K}\cdot\tilde{\boldsymbol{E}}(\boldsymbol{k},\omega)=-\mu_0\omega\tilde{\boldsymbol{J}}_{Ext}(\boldsymbol{k},\omega),\tag{3}$$

with $k_0=\omega/c$, and the plasma dielectric tensor comprises the sum of the cold and warm components. In a cold ($T_e=T_i=0$) plasma, the dielectric tensor with $\mathbf{B}_0$ along the z-axis is given by

$$\boldsymbol{K}=\begin{bmatrix}K_{xx}&K_{xy}&0\\-K_{xy}&K_{xx}&0\\0&0&K_{zz}\end{bmatrix},\quad K_{xx}=1-\sum_j\frac{\omega_{pj}^2}{\omega^2-\omega_{cj}^2},$$
$$K_{xy}=-i\sum_j\frac{\dfrac{\omega_{cj}\omega_{pj}^2q_j}{|q_j|}}{\omega\left(\omega^2-\omega_{cj}^2\right)},\quad K_{zz}=1-\sum_j\frac{\omega_{pj}^2}{\omega^2},\tag{4}$$

and ω_{cj}, ω_{pj}, and q_j are the cyclotron frequencies, plasma frequencies, and charge, respectively, of plasma species j. Setting the left side of (3) to zero and using (4) yields a dispersion equation $D(\mathbf{k},\omega)=0$ for the linear waves that propagate in a cold, magnetized plasma. With a nonzero ion and electron temperature, the warm dielectric tensor $\boldsymbol{K}$ depends on the ion acoustic wave speed[20–22,41] found from $c_s^2=(\kappa T_e+3kT_i)/m_i$.

Figure 13 provides a sample solution to illustrate typical ionospheric parameters including warm plasma dispersion $\omega(\mathbf{k})$ for oblique propagation relative to the magnetic field vector $\mathbf{B}_0$. The plasma waves lie on distinct branches with a change in mode for frequencies below and above the ion cyclotron frequency ω_{ci}. In a cold plasma, the slow magnetosonic, ion acoustic, ion sound branches vanish.

The labels on the three curves in Fig. 13 indicate individual modes that may propagate from a satellite as either linear waves or nonlinear solitons and shocks. The solitons may be produced for modes with nonlinear dispersion. The linear plasma waves propagate with group and phase velocities, $\boldsymbol{v}_g=\nabla_{\boldsymbol{k}}\omega(\boldsymbol{k})$ and $v_p=\omega(\boldsymbol{k})/|\boldsymbol{k}|$, respectively, which can be found from the slope and values of the dispersion curves. For the electrostatic solutions to (2), the electric field is the gradient of a potential, i.e., using $\boldsymbol{E}=-\nabla\phi$. The electrostatic

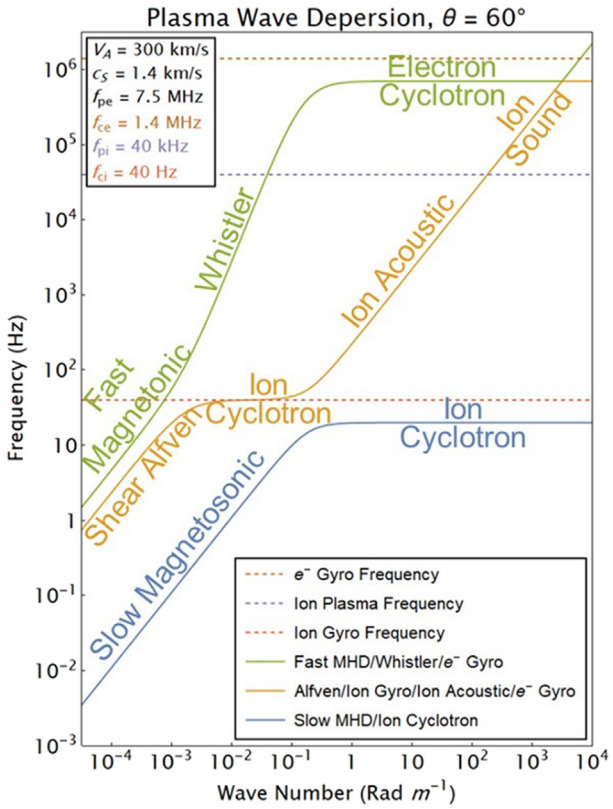

FIG. 13. Dispersion relation of waves in a warm fluid plasma with oblique propagation for representative ionospheric conditions. The waves lie on three distinct (green, orange, and blue) branches over a wide range of frequency and wave numbers. Electrostatic waves are found on the horizontal portions of the curves near the ion gyro and electron gyro frequencies. The electrostatic ion acoustic and slow magnetosonic modes are not contained in Eq. (4), and this dispersion is for a single ion O^+ species. The ion acoustic mode makes a transition to heavily damped ion sound mode after crossing the ion plasma frequency.[22,40]

regions in Fig. 13 are the horizontal portions of the curves near the ion and electron cyclotron frequencies and the large-wavenumber regions of ion acoustic and magneto-acoustic waves.

Fields with large amplitudes drive the solutions to higher order for electric fields, densities, currents, velocities, pressures, etc. Second order solutions to (2) show the impact of group velocities on the electric field amplitudes in a medium with nonlinear dispersion.[43,44] Third and higher order solutions yield solitons[22,43] and vortex systems[43] from Eq. (2) as waves propagate relative to the phase speed of linear waves. The nonlinear forms of (2) for isotropic, ion-acoustic wave solitons (a) have often neglected the ambient magnetic field, collisions, and Landau damping, (b) have discarded EM effects by using an electric potential, and (c) are only valid for frequencies above the ion cyclotron frequency. The Alfvén and magnetosonic (both fast and slow) soliton solutions are applicable below the ion cyclotron frequency. Table III is a list of plasma wave descriptions for the Nonlinear Schrödinger (NLS),[20,43–46] Korteweg–de Vries (KdV),[1–3,5–8,10–16,20,22,26,42–48] and Pseudopotential Well[42–44,49,50] equations with closed form solutions. The KdV Equation with Landau damping produces a soliton with a decay of an initial perturbation.[13,51,52] The variable ψ can represent density, velocity, electric potential, and wave magnetic field of electromagnetic waves. The electrostatic electric field is derived from the spatial derivative of the electrostatic potential.

Theoretical predictions related to spacecraft-driven waves have focused on *nonlinear* waves such as ion acoustic solitons[1,2,5–7,10,12,13,15,30] with no magnetic field and magnetosonic solitons[1,11,14,16,53] with no consideration of the ion cyclotron and lower hybrid frequency limits to the ion acoustic, slow, and fast magnetosonic waves. The STS-127 experiment data (Fig. 2) and the Swarm-E/RRI data (Figs. 6–13) suggest that the Fast Magnetoionic wave, the Electrostatic Lower Hybrid wave, and, to a lesser degree, the Ion Acoustic wave may be important sources of satellite plasma waves.

The nonlinear electric field solutions are classified as pinned or lump if they travel with the space object and as precursors if they travel in the orbit direction away from the source. These types of plasma wave environments are discussed in the next two sections.

A. Steady state disturbances moving with charged space objects in orbit

The pinned solitons are continuously sustained by the charged object motion that are steady solutions in the reference frame of the object orbit. These are steady state solutions of nonlinear electric field equations[16] and they are found close to the charged object to within a few Debye lengths[10] or electron skin depths[48] or ion inertial lengths.[16]

Electric field sensors passing through a region of electric fields attached to a charged source could represent the *in situ* observations. For this, the primary consideration for finding of space objects using

TABLE III. Nonlinear equations for propagating solitary waves in a plasma.

Equation	Nonlinear form	Soliton solution	Waves
Nonlinear Schrodinger	$i\frac{d\psi}{dt} + P\frac{d^2\psi}{dz^2} + Q\lvert\psi\rvert^2\psi = 0$	$\psi = \frac{\sqrt{2\eta}}{L}\operatorname{sech}\left(\frac{z-Ut}{L}\right)e^{i\theta}$	IA, Alfven, Langmuir
Korteweg-de Vries	$A\frac{d\psi}{dt} + \frac{1}{2}\frac{d^3\psi}{dz^3} + B\psi\frac{d\psi}{dz} = 0$	$\psi\frac{3U/A}{B}\operatorname{sech}^2[\sqrt{\frac{UA}{2}}(z-Ut)]$	IA, Alfven fast–slow magnetosonic
Pseudopotential well	$\frac{1}{2}(\frac{d\psi}{dz})^2 + \Phi(\psi, V) = 0$	$\psi = \psi_m \operatorname{sech}^{l(\psi_m)}[z/\Delta(\psi_m)]$	IA, Alfven, whistler fast–slow magnetosonic
	$\Phi(\psi, V) = 1 - e^{\psi}V^2\left(1 - \sqrt{\frac{2\psi}{V^2}}\right)$		

plasma waves is the scale of the electric field disturbance that extends from the object. If the motion-induced plasma oscillations are located near a piece of space debris, an *in situ* sensor would be in danger of being struck by the debris. Estimations of the extent of the plasma waves around a space vehicle are required to determine its observability. The dimensions of plasma disturbances are characterized by spatial scales associated with the ratio of a characteristic velocity to the wave mode frequency. Table IV is a list of standard kinetic and inertial scale lengths in a typical plasma found at altitudes of satellites in low earth orbit. These scale lengths are listed in order of size and can be related to both unmagnetized and magnetized plasma wave modes.

The shortest scale in Table IV is the Debye length which is associated with both nonlinear ion acoustic waves and nonlinear electron-plasma (Langmuir) waves.[54] Strong Langmuir turbulence (SLT) in the ionosphere from a vertically directed beam of high-power radio waves has been used to explain caviton generation[21,55] detected by incoherent scatter radars.[54,56] Caviton collapse during SLT is related to parametric instabilities[57] and is responsible for the electron acceleration and for the intense optical emission from the perturbed regions of the ionosphere.[58–61]

Ion acoustic density enhancements in the form of both lump or pinned solitons have been predicted with many computer simulations and laboratory experiments.[1–16] All of the analysis for electrostatic precursor solitons without Landau damping is only applicable for propagation of the Slow Magnetosonic wave along magnetic field lines,[22] and even these can be strongly dissipated if the ion temperature is above the electron temperature.[62] For propagation across magnetic field lines, ion acoustic waves need to be simulated with a lower frequency limit of the ion cyclotron frequency and with Landau damping.[22] The limitation in observing pinned ion acoustic solitons from space debris is that their spatial distance is only a few centimeters (Debye lengths) from the target. Probably the best way of measuring nonlinear ion acoustic waves generated by space debris is with a radar transmission that matches the wave number (or wavelength) of the ion acoustic wave mode. The limitation of the ion acoustic wave radar scatter is that the space debris has a radar cross section of the same size as the ion acoustic wave disturbance attached to the target. Because the satellite-generated ion acoustic waves (1) are at the ion acoustic velocity which is small around 1 km/s, (2) are attenuated by Landau damping, and (3) do not exist for frequencies below the ion cyclotron frequency (see Fig. 13), it is apparent that there may be little chance of observing ion acoustic wave solitons with either *in situ* observations or radar scatter. This conclusion is borne out with the observations of Sec. IV B, which has no evidence of ion acoustic waves based on electric field polarization and frequency range.

The intermediate distances for the ion gyroradius (~5 m) were presented earlier represent lower hybrid waves generated by diamagnetic drifts across magnetic fields in spacecraft wakes (Fig. 5). The electrostatic lower-hybrid waves may be launched simultaneously with electromagnetic magnetosonic waves that propagate across magnetic field lines. The electron skin depth is associated with the shear Alfvén cross field dimension.[63–66] UHF radars have been used to observe lower hybrid waves excited by satellite rocket burns when the plume travels far enough from the satellite to prevent direct target scatter.[67,70]

The largest scale given by Table IV is the is ion inertial length[16,71] which is applicable to both the shear[63,64] and compression Alfvén wave disturbances.[66] In addition, of all the waves listed in Table I, the transverse compressional Alfvén (i.e., TCA or fast magnetosonic) and lower-hybrid (i.e., LH) waves are the most often observed by operations of spacecraft in the ionosphere.[72] Electric fields from these waves have been attributed to on-orbit rocket motor burns[23] (Fig. 2), locally excited spacecraft emissions[29] (Fig. 5) and the FLASH burst observations clearly illustrated in Figs. 6–12. A common feature of the TCA and LH modes is that they are found on the same frequency vs wave number dispersion curve for a magnetized plasma for propagation nearly perpendicular to $\mathbf{B}_0$ (Fig. 14).

Objects in orbit travel much slower than the Alvén speed and the spacecraft driven Alfvén waves must either be linear disturbances or pinned electromagnetic solitons with limited extension along magnetic field lines.[16] The most plausible theory for generation of the linear waves is the Cherenkov mechanism. All the observations are consistent with the excitation of compressional Alfvén (fast magnetosonic) waves with their frequency limited by the local value of lower hybrid wave around 8 kHz in the ionosphere. Cherenkov radiation generated by charged spacecraft can propagate along, oblique, and transverse to

TABLE IV. Plasma scale lengths around charged space objects in low earth orbit.

Quantity	Formula	Typical value	Speeds, frequencies
Debye length:	$\lambda_D = \sqrt{\frac{\varepsilon_0 k T_e}{q_e^2 n_e}} = \frac{v_{th,e}}{\omega_{pe}}$	~1 cm	$v_{th,e}^2 = \frac{kT_e}{m_e}, \omega_{pe}^2 = \frac{q_e^2 n_e}{\varepsilon_0 m_e}$
Electron gyro radius:	$r_e = \frac{v_{th,e} m_e}{q_e B_0} = \frac{v_{th,e}}{\omega_{ce}}$	~10 cm	$\omega_{ce} = \frac{q_e B}{m_e}$
Ion gyro radius:	$r_i = \frac{v_{th,i} m_i}{q_i B_0} = \frac{v_{th,i}}{\omega_{ci}}$	~3 m	$v_{th,i}^2 = \frac{kT_i}{m_i}, \omega_{ci} = \frac{q_i B}{m_i}$
Ion sound gyro radius:	$r_s = \frac{c_s m_i}{q_i B_0} = \frac{c_s}{\omega_{ci}}$	~5 m	$c_s^2 = \frac{kT_e}{m_i}, \omega_{ci} = \frac{q_i B}{m_i}$
Electron skin depth:	$d_e = \sqrt{\frac{m_e}{n_e q_e^2 \mu_0}} = \frac{c}{\omega_{pe}}$	~10 m	$\omega_{pi}^2 = \frac{q_i^2 n_i}{\varepsilon_0 m_i}$
Ion inertial length:	$d_i = \sqrt{\frac{m_i}{n_i q_i^2 \mu_0}} = \frac{c}{\omega_{pi}} = \frac{v_A}{\omega_{ci}}$	~2 km	$v_A = \sqrt{\frac{B_0}{\mu_0 m_i n_i}} = c\frac{\omega_{ci}}{\omega_{pi}}$

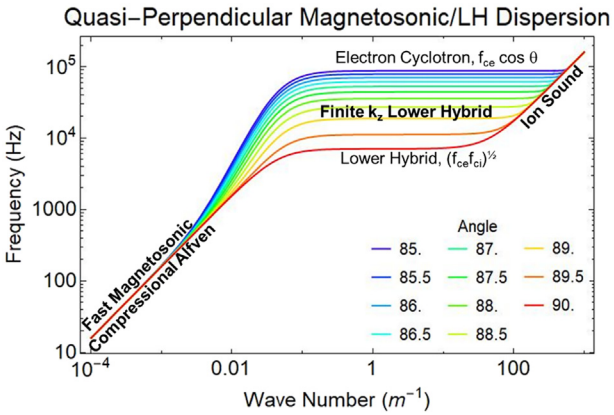

FIG. 14. Waves from satellite proximity conjunctions have the characteristics of transverse compressional Alfvén (TCA) and finite k_z lower hybrid (LH) waves with transitions to ion sound waves at the shortest wavelength. Dispersion for these curves assumes a warm plasma and that propagation at an angle θ with $\mathbf{B}_0$ near 90°.

the ambient magnetic field. For the classic Cherenkov process, a moving charge plays the role of an antenna that excites waves whose properties are determined by a background plasma dielectric.[73] Excitation of shear Alfvén waves by this process will be computed using the model based on Eq. (3) with only the diagonal components of the dielectric tensor (4) for frequencies below the ion cyclotron frequency.[63,64] In space plasmas, two ion species are often found between the O^+ dominated regions below 500 km and the H^+ plasmasphere above 1000 km altitude. Under these conditions, the simulation of Cherenkov excitation of shear Alfvén waves will be limited to charges moving either along and across $\mathbf{B}_0$. Parallel motion uses simplified 2D cylindrical geometry.[63,64] For perpendicular motion, the integrated disturbance is computed along the coordinate transverse to both the satellite velocity x-direction and the magnetic field z-direction.

The Cherenkov process Is considered for magnetohydrodynamic (MHD) turbulence generated by time-varying currents in a magnetized plasma. Excitation of shear Alfvén waves is in the inertial limit, where the Alfvén speed, v_A, is much larger than the electron thermal speed of the plasma. These linear wave simulations have debris motion along orbit in one direction but, unlike one-dimensional nonlinear soliton models,[1–16] they provide description of the resulting disturbance in both longitudinal and transverse directions. Figure 15(a) shows simulation results in the cylindrical geometry for the inverse Fourier transform of Eq. (3). The simulation parameters represent localized charged space debris moving through a background plasma along the magnetic field with the spatial-temporal evolution of the current density with a Gaussian cross section is described by the following equation:

$$J_{zExt} = V_{Sat} q N_b \frac{\Omega_i}{\pi V_A d_\perp^2} \delta\left[\frac{\Omega_i}{V_A}(z' - V_{Sat}t)\right] \exp\left(-\frac{r'^2}{d_\perp^2}\right) z',$$

where

$$\Omega_i = \frac{eB_0}{m_i}, \quad V_A = \frac{c\Omega_i}{\omega_{pi}}, \quad \omega_{pi}^2 = \frac{q^2 N_i}{\varepsilon_0 m_i}, \tag{5}$$

where N_b is the number of electric charges q, V_{at} is the velocity, z′ is the direction along the trajectory, r′ is the radial dimension across the orbit, $d_\perp$ is the size of the object, Ω_i is the ion gyro radius around a magnetic field line $\mathbf{B}_0$, and V_A is the Alfvén speed. The simulation parameters are $d_\perp = 1$ m, $V_{Sat} = 7.0$ km/s, $J_{zMax} = N_b q V_{Sat}$, $V_A = c\Omega_i/\omega_{pi} = 538$ km/s, $v_e = (kT_e/m_e)^{1/2} = 213$ km/s, $\lambda_e = c/\omega_{pe} = 19$m, $L_{IE} = V_A/\Omega_i = 2.9$ km, $\rho_s = c_s/\Omega_i = 6.7$ m, and the species is O^+ ions. The spacecraft current source for Cherenkov calculations is $\mathbf{J}_{zExt}$ given by Eq. (5) with z′ = z the magnetic field direction. The actual source current depends on spacecraft charging processes which vary with the object of interest. The charging processes were not included so all computed currents are normalized to J_{zMax}.

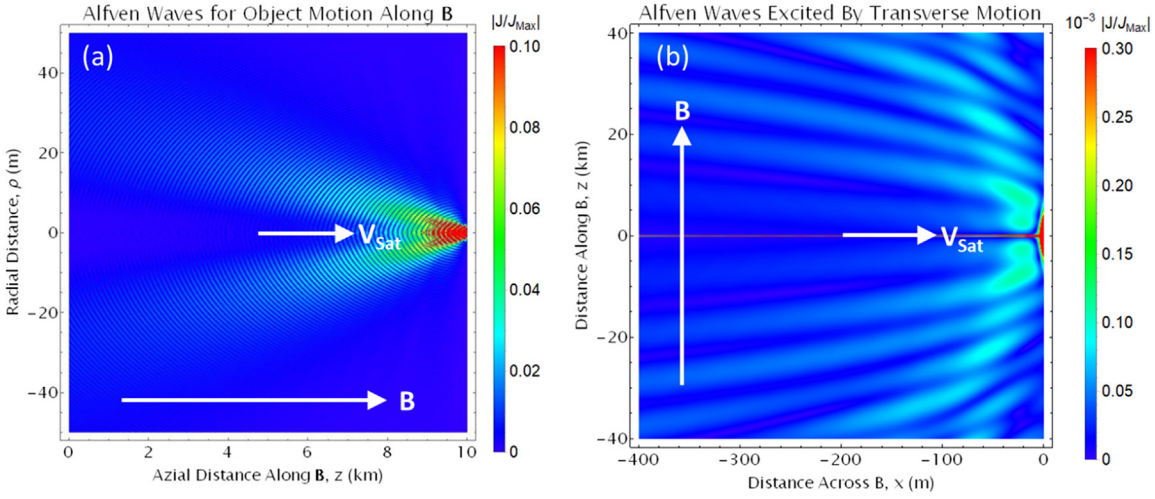

FIG. 15. Numerically Simulated Cherenkov radiation for currents associated with shear Alfvén waves from the space debris in orbit (a) along and (b) across magnetic field lines. The charged space debris is at the point of maximum current along the orbit in both cases. Note the change in spatial scales between parts (a) and (b). The satellite is shifted in position to (a) z = 10 km and (b) z = 0 km.

The vertical scale of Fig. 15(a) is expanded relative to the coordinates of the motion along B showing waves that can be found in a narrow channel behind the space debris out to ranges of 25 km or more. This distance, associated with the ion inertial scale, is much larger than that predicted by three-dimensional simulations of pinned ion acoustic solitons[3] but is consistent with results from one-dimensional simulations of pinned Alfvén MHD solitons.[16] For the shear Alfvén waves in Fig. 15(a), the cross-B scale is the electron skin depth defined in Table IV and is also much larger than the Debye length scale associated with ion acoustic waves.

When the charged space object travels perpendicular to the magnetic field, the range of the disturbances are extended to even larger distances [Fig. 15(b)]. For this calculation, the spacecraft current source cross section given by the Inverse Transform of a Lorentzian function as

$$\boldsymbol{J}_{xExt} = V_{Sat} q N_b \frac{\Omega_i}{V_A 4 d_\perp^2} \delta\left[\frac{\Omega_i}{V_A}(x' - V_{Sat} t)\right] \exp\left(-\frac{|y'| + |z'|}{d_\perp}\right) \boldsymbol{x}', \tag{6}$$

where z′ is the dimension along the magnetic field and x′ is the direction along the trajectory and across **B**. The simulation is made in the orbit-field (x, z) plane with the y-dimension eliminated with a spatial integral along the y-direction by setting $k_y = 0$. The large charge induced current at the spacecraft excites Alfvén Waves that extend many kilometers along the magnetic field lines and trail behind for a few hundred meters. The out-of-plane (y-axis) disturbance also expands to a few hundred meters. Such an expanse of shear Alfvén waves is much easier to detect with an *in situ* probe than are the waves produced by orbital motion along B-field lines.

Space plasmas have multiple ions. In low earth orbit between about 200 to 600 km altitude, the ionosphere is typically dominated by atomic oxygen (O^+) ions and the single ion theory illustrated in Fig. 16 is appropriate. At higher altitudes up to 2000 km, the plasmasphere is usually composed of both atomic oxygen and hydrogen (H^+) ions. The Cherenkov radiation of shear Alfvén waves in a plasma has been simulated[64] with a multiple-ion implementation of Eq. (3). With the addition of a second ion, the Alfvénic wake of charged spacecraft will yield an additional frequency range involving the ion–ion hybrid frequency and the cyclotron frequency of the lighter species, but the disturbance is expected to be launched for tens of km from the space debris.

It is clear that a three-dimensional Cherenkov model for charged space objects should be used with a source current representation (6) directed along the **x**-axis perpendicular to $\mathbf{B}_0$. Unlike the shear Alfvén wave, however, the compressional Alfvén wave in a cold plasma is isotropic and, for Cherenkov radiation, the speed of the charge particle needs to be larger than the phase velocity of the wave in the media.[73] Therefore, for a moving charge to excite, this mode the velocity must be larger than the Alfvén speed, which is not the case for satellites.

In summary, the appropriate source for waves generated by charged space debris in space plasmas is probably not the ion acoustic or magnetosonic solitons but could be Cherenkov-like radiation[63,64] applied to the dispersion branch of compressional Alfvén and lower hybrid waves (Fig. 15) from cross field motion. The lower hybrid waves can also be excited by the Lower Hybrid Drift Instability. Space object motion across magnetic field lines is required to excite the observed electromagnetic waves. Only linear waves are considered because magnetosonic soliton generation is not possible with a spacecraft velocity (∼7 km/s) that is well below the Alfvén speed (∼400 km/s) in a space plasma. Fortunately, the Cherenkov model is valid for charged object speeds less than the Alfvén speed.[63,64] The upper frequency limit for compressional Alfvén waves is the ambient lower hybrid frequency as shown by the dispersion curves for these waves in Fig. 15. The ambient plasma dielectric with this LH wave limitation will be added to the existing Cherenkov model by changing the plasma wave dispersion

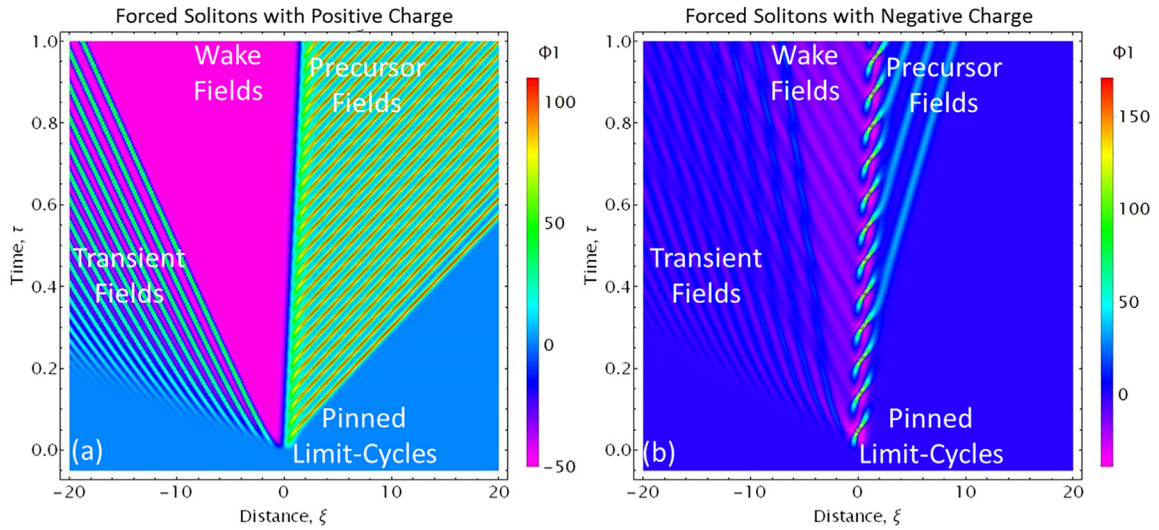

FIG. 16. Simulations of the electric potential on an orbiting object that is (a) positively or (b) negatively charged starting at time $\tau = 0$. Space objects will be negatively charged in the ionosphere and the response of (a) is much more representative than that of (b).

function currently in the simulation code. This enhanced linear wave theory may explain the RRI wave measurements shown in the experiment section of this paper.

B. Transient disturbances launched from moving charged space objects

Next consider a space object with charges that change in time. Temporal changes of electric charge on a spacecraft or space debris can drive both linear and nonlinear plasma waves to radiate in the reference frame of the object. Precursor solitons can be generated by an initial condition, a transient event, or a temporal fluctuations at the space object. These transient and temporal events could be a sudden change in electric charge, current, pressure, or neutral velocity.

To illustrate this temporal nature, the ion acoustic soliton model of Sen *et al.*[3] is employed with considerations of the full range of nonlinear dynamics solutions to the Korteweg–de Vries equation,

$$\begin{aligned} &\Phi(\xi,\tau)=N(\xi,\tau)=U(\xi,\tau), \quad U_{ph}=1 \\ &\frac{\partial\Phi(\xi,\tau)}{\partial\tau}+\Phi(\xi,\tau)\frac{\partial\Phi(\xi,\tau)}{\partial\xi}+\frac{1}{2}\frac{\partial^3\Phi(\xi,\tau)}{\partial\xi^3} \\ &=\frac{1}{2}\frac{\partial S_2[\xi+(1-V_d)\tau]}{\partial\xi}, \end{aligned} \tag{7}$$

where ambient electron density, Debye length, ion acoustic speed, and electron thermal plasma potential,

$$n_0, \quad \lambda_D=\sqrt{\frac{\varepsilon_0 kT_e}{e^2 n_0}}, \quad c_S=\sqrt{\frac{kT_e}{m_i}}, \quad \omega_{pi}=\sqrt{\frac{e^2 n_0}{\varepsilon_0 m_i}}, \quad \phi_e=\frac{kT_e}{e}, \tag{8}$$

are used to normalize distance, time, electric potential, ion velocity, and disturbed plasma density by

$$\begin{aligned} &X=\frac{x}{\lambda_D}, \quad T=\frac{c_s}{\lambda_D}t=\omega_{pi}t, \quad \Phi(X,T)=\frac{\phi(x,t)}{\phi_e}, \\ &U(X,T)=\frac{u(x,t)}{c_S}, \quad N(X,T)=\frac{n(x,t)}{n_0}, \end{aligned} \tag{9}$$

and spatial coordinate is stretched by the ion acoustic phase speed with $\xi=X-U_{ph}T$ and $\tau=\omega_{pi}t=T$.

The charge forcing function is the external object current in (1) divided by the object speed in the form a Gaussian function,

$$S_2[\xi+(1-V_d)\tau]=Ae^{-\left[\frac{\xi+(1-V_d)\tau}{G}\right]^2}, \tag{10}$$

where G is the spatial size dimension and A is the negative charge. The forced KdV equation has been used by a number of authors, The important factors for these solutions are the magnitude and sign of the object charge A, the initial conditions for the charge source and the field disturbance at the start of the simulation, the size G of the charged object, and the spatial boundary conditions. Previous work has displayed the results of simulations to show precursor ion acoustic solitons and trailing wake disturbances[3,6,9,10] for charge objects. Those results are duplicated here with the additional emphasis of wake field transients and pinned oscillations for both positively and negatively charged spacecraft.

The normalized KdV equation (7) is solved numerically with Gaussian forcing (10) for periodic and absorption boundary conditions. The results are displayed in Fig. 16 in distance vs time coordinates to show (1) transient trailing fields triggered at the time of initial charging, (2) localized limit cycles near the object inside the source charged region, (3) cavitons trailing behind the object, and (4) precursor ion acoustic solitons launched at the forward boundary of the charged object by the limit cycle oscillations. Figure 16 shows the potentials for both negatively and positively charged space objects in a spatial-temporal format. At the time of charging, transient solitons are launched in the wake of the object. Also in the wake is a region of negative potential expanding from the object which is either (a) uniform or (b) structured with cavitons depending on the charge sign. Near the object in the charged region, limit cycle oscillations are found with time periods that decrease with increasing charge. Precursor solitons are launched in the ram direction from the limit cycle oscillations.

It is well known that spacecraft charging in the ionosphere is nearly always negative unless an electron gun is used to remove electrons from the object.[70–72] Figure 16 shows that assuming positive charge for a negatively charged object will produce large errors in the orbit driven waves especially for the growth and detachment of precursor solitons. Previous theoretical work that use positively charged spacecraft should be examined for validity. This contrast of ion acoustic soliton generation the sudden introduction of both positive and negative charges is presented here for the first time. The most important step for future research is self-consistent modeling of both object surface ionization to yield the correct excitation of electromagnetic plasma waves.

Detailed modeling is required for accurate spacecraft charging.[67–69] The charge state of an object depends on photo emission of electrons by sunlight or electron collection by attachment of ambient electrons. Thus, precursor soliton production could be change during the motion of the space object from darkness to sunlight across the Earth's terminator boundary or could be excited by a change in charge if the space object passes through an irregular electron structure in the ambient plasma. Rapid change between low-level and high-level negative charging that results from modest changes in the spacecraft charging conditions is essential to the generation of precursor solitons but is beyond the scope of this paper.

The example in Fig. 16 is representative of models for plasma waves are derived from an initial boundary value problem solution to non-linear equations derived from plasma fluid equations[10] or particle-in-cell (PIC) simulations.[48] For precursor ion acoustic solitons, the nonlinear equation is derived from continuity, momentum, and Poisson's equation, where magnetic fields have been neglected. Nonlinear models[5–8,10,13] that start with zero initial amplitude and have a sudden introduction of charge at t = 0 produce the precursor solitons that propagate away from the space debris. It is not surprising that if, at t = 0, the charge on the object suddenly changes, it can launch a trailing disturbance. This, however, will occur only once at a transition time for the space object and will not be repeated unless some other transient space event occurs.

For PIC simulations of slow and fast magnetosonic waves, the startup scenario is a high-velocity ion beam instantly appearing at time t = 0 in the plasma.[48] In both the ion acoustic and magnetosonic simulations, the precursor solitons are generated by the instantaneous appearance of the charged space object. In reality, spacecraft charging

time is dependent on the charging process and is not instantaneous. Also, for precursor solitons to be useful, they must be sporadically regenerated as transient events in space. In steady state, charged space debris do not generate precursor solitons.

The Korteweg–de Vries equation, such as given by (7), applies to any nonlinear wave balanced by dispersion terms and has a general representation of

$$\text{KdV Equation}: \frac{\partial b}{\partial t} + a\frac{\partial b}{\partial x} + Nb\frac{\partial b}{\partial x} + \beta\frac{\partial^3 b}{\partial x^3} = 0, \qquad (11)$$
$$a = V_g, \quad N = \text{Nonlinearity}, \quad \beta = \text{Dispersion}.$$

In addition to ion acoustic waves, the KdV equation can be applied to nonlinear Alfvén waves which propagate near the Alfvén speed at low frequency and long wavelength, and begin to show dispersion near the ion cyclotron frequency[22,46] as shear Alfvén wave solitons. The KdV equation also applies to fast and slow magnetosonic waves.

A transient event example for a precursor *soliton* mode may have been observed as the compressional Alfvén wave in Fig. 2. For this event, Space Shuttle OMS engines were operated for 10 s to establish steady state and they were instantly turned off to provide a transient change in the plasma forcing pressure and neutral velocity.[23] This change in local neutral velocity couples to the plasma through the neutral collision frequency ν_n in (2). This MHD pulse required a large amplitude temporal change in the nozzle pressure and velocity of large OMS rocket motors in low earth orbit. The resulting pulse, traveling at the speed of the fast magnetosonic wave near 400 km/s, was a precursor to the arrival of the supersonic exhaust cloud traveling at about 6 km/s. This is similar to the transient excitation of magnetosonic solitons in plasma in the presence of an external magnetic field by a short laser pulse normal to an over dense plasma target.[47] All precursor solitons from space objects require transient changes in object charge density or, in the case of satellites, an ignition of an ion or chemical thruster to produce a transient in the ion velocity. Modeling of precursor solitons with a charged object initial condition in a quiescent plasma is equivalent to introducing a step function change in electric charge during a time-dependent simulation. The precursor soliton is launched by the time derivative of the charge state not the charge state itself.

The analytic solution to the KdV equation (11) given by $b(x,t) = \frac{3c}{N}\text{sech}^2[\frac{c^{1/2}}{2\beta^{1/2}}(x - at - ct)]$ is shown in Fig. 17. No such

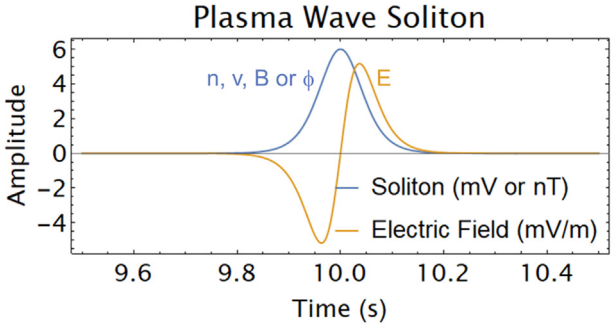

FIG. 17. KdV equation solution for a solitary wave for that resembles the compressional Alfvén wave measured during the STS-127 mission with C/NOFS shown in Fig. 2.

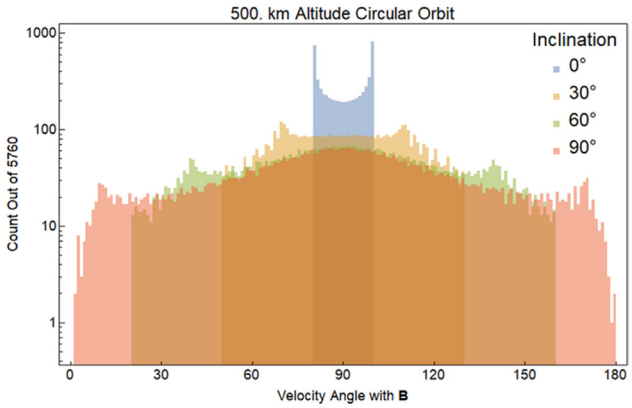

FIG. 18. Computation showing that all satellite orbits cross magnetic field lines at 90°. The near normal orbits excite fast magnetosonic and lower hybrid waves that can be used to observe waves from space debris.

solitons were observed during the observations with Swarm-E but, with selected parameters, can produce a close resemblance to Fig. 2 for the sudden termination of a rocket motor in a plasma. All the electric-field data recorded for passes near other spacecraft can be attributed to linear waves.

Both theory and particle simulations indicate that the threshold for generation of electrostatic solitons requires that the wave source moves with a speed (V_b) greater than the linear group velocity of each type of plasma wave mode. For space objects in low earth orbit near 7 km/s, this is easily accomplished for the isotropic ion acoustic and slow magnetosonic modes around 1 km/s is apparently not impossible for excitation of Shear and Compressional Alfvén waves with phase and group velocities around 100 to 500 km/s.

Electromagnetic precursor and pinned solitons are generated even when V_b is less than the Alfvén speed V_{ms} but they are considerably weaker than the $V_b > V_{ms}$ case.[48] For pinned solitons, numerical investigations[16] show that Alfvén solitons in a cold plasma only exist for $V_b < V_A$ and a warm plasma is required to have soliton solutions for $V_b > V_A$. Pinned soliton simulations show disturbances within a few ion inertial distances of the space object.[16] Sub-Alfvénic generation of low frequency, ion-inertial waves for objects moving nearly perpendicularly to **B** have been simulated by Sen *et al.*[16] These waves may be detected *in situ* with a sensitive magnetometer such as e-POP Magnetic Field Instrument (MGF).

V. MEASUREMENT GEOMETRY FOR REMOTE EXCITATION OF ORBIT DRIVEN PLASMA WAVES

The plasma wave generation by charged space objects seems to require motion across magnetic field lines. The angle between $\mathbf{V}_{Sat}$ and $\mathbf{B}_0$ depends on the inclination of the orbit, the structure of the Earth's magnetic field and, to a lesser degree, the altitude of the orbit. Figure 18 is a model simulation for the distribution of magnetic field incidence angles for satellites at 500 km altitude and 0°, 30°, 60°, and 90° inclinations. This model uses a tilted dipole for the ambient magnetic field.[74,75] Cross field motion occurs at the highest latitude points in any orbit. The lower inclination orbits that spend a longer fraction of time traversing magnetic field lines at high angles should be easier to detect using motion-driven compressional-Alfvén (CA) waves.

The bulk of satellites and space debris is found with mid to high inclination orbits (Fig. 19).

The observations of plasma waves generated by charged spacecraft can be made with either (a) *in situ* probes or (b) scattering of electromagnetic waves. First, at close proximity, waves from a space object could be sensed with an electric field sensor on a small satellite that penetrates the Spreading Trail of MHD waves similar to that shown in Fig. 15(b). This would require that one or more host satellite pass within 100 to 25 000 m of the target object radiating MHD waves with known magnetic field geometry. Space debris with a plasma wave envelope of compressional Alfvén waves can be observed with *in situ* electric and magnetic field sensors with dipole probes such as found on the Swarm-E satellite. The Swarm-E satellite typically collects electric field data for up to ten minutes when it is predicted to fly close to other known satellites and space debris. The planning of such conjunctions should also consider if the target object is crossing magnetic field lines at nearly normal incidence to favor excitation of the compressional Alfvén branch of plasma waves.

Second, the charged space object that is emitting plasma waves could pass through a region of the ionosphere illuminated by high power electromagnetic waves, which are scattered to the ground. This is similar to optical measurements of small space debris with scatter by 1-W laser beam in a disk that is about 100 m of less in radius.[76] This approach to space debris observations is to scatter electromagnetic waves from the plasma oscillations that accompanies the target object. The stimulated scatter technique could use a ground HF transmitter, such HAARP in Alaska[77] or EISCAT in Norway,[54] to illuminate the bottomside F-region with high power electromagnetic radiation that could mix with satellite generated waves and scatter an electromagnetic wave back to a ground receiver. This process is related to stimulated electromagnetic emissions (SEE) including stimulated Brillouin scatter of magnetized ion acoustic and ion cyclotron waves[78,79] and of injected probe waves.[80] In this application of Brillouin scatter, the satellite would provide the injected wave that yields a frequency shift in the scattered signal. Data from an array of ground-based receiver antennas could provide an image of a charged space object passing through the HF beam (Fig. 20).

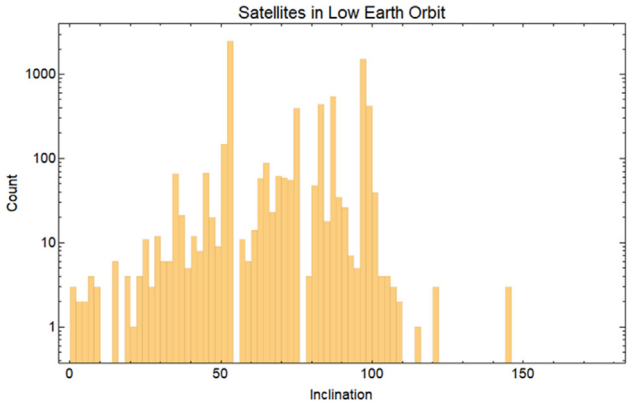

FIG. 19. Distribution of satellite inclinations for LEO orbits. The bulk of space objects are clustered near 52° for midlatitude applications and 98° for sun synchronous applications. Most space debris are found with inclinations between 80° and 100°.

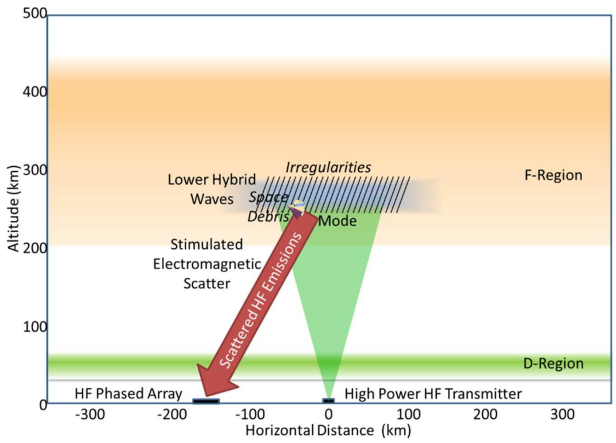

FIG. 20. Space debris passing through HF driven plasma for wave diagnostics of stimulated electromagnetic scatter (SES). The received frequency spectrum would provide the time that the target object passes though the HF inaction region. Both stimulated scatter and field aligned irregularities can play a role in wave measurements.

The field aligned irregularities associated with high power HF waves[77] could affect the charging of the satellite. As discussed in Sec. IV, these temporal variations in object charge can launch both linear and nonlinear waves in the reference frame of the orbit to be measured by other spacecraft and scatter from incident electromagnetic waves.

The stimulated electromagnetic scatter could provide a signal from a small (i.e., 1 cm) object because the plasma wave Spreading Trail traveling with the object could be much larger (i.e., 50 km) in size. The Rayleigh scatter of an HF (i.e., 5 MHz) wave is not detectable because radar cross section vanishes for radio wavelength (i.e., 60 m) much larger than the object. The stimulated electromagnetic scatter (SES) process, represented by Eq. (1), can be highly efficient if the satellite waves seed a parametric decay process that amplifies the seed waves. A diagram of this process is given by Fig. 21.

Stimulated electromagnetic emissions (SEE) are a proxy for stimulated EM scatter (SES) from the plasma wave environments around spacecraft. The scatter process of Eq. (1) occurs spontaneously for SEE and is driven by the satellite wave environment for SES. Figure 22 shows the wide variety of sidebands produced when electrostatic and electromagnetic waves interact with a high-power HF pump waves. The concept of SES is that additional sidebands will appear in the backscatter EM spectrum as a satellite passes through the HF interaction volume.

The stimulated scatter process is only proposed for determination of plasma waves produced by the space object not for detection of new space objects. There are 34 satellites available with high inclination and low altitude to pass through the HAARP modification region over Gakona, Alaska. Swarm-E is one of these satellites. The satellite generated downshifted sidebands would appear for only the 10 or less seconds that the satellite passes through the HAARP HF beam and thus could be distinguished from those naturally generated parametric decay process. This concept of ground observations of satellite generated plasma waves will be the subject of a future paper with both theoretical simulations and experimental validation.

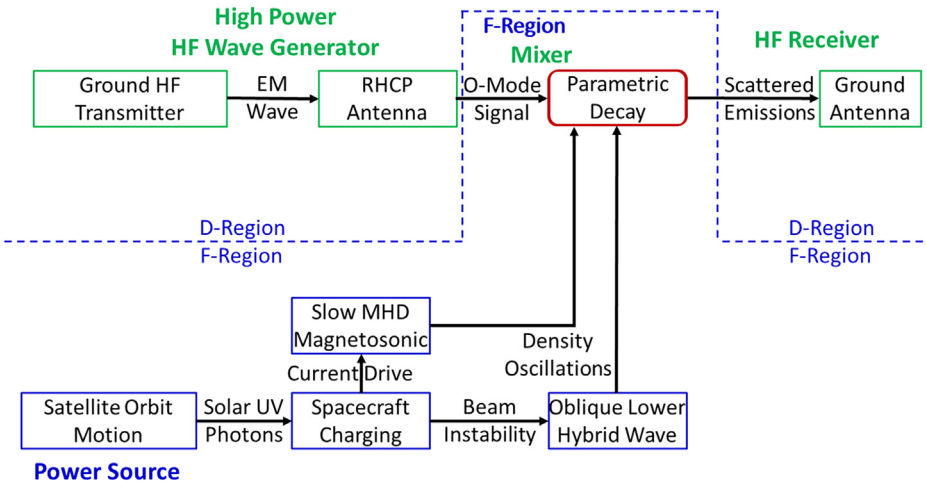

FIG. 21. Remote observation of waves from space debris in low earth orbit by stimulated scatter of high power HF waves from ground transmitters.

VI. CONCLUSIONS

The observational results of this paper have provided tests and partial validation for theories of plasma wave generation by space objects. It has been proposed by other authors that solitary structures from either isotropic, ion-acoustic waves above the ion gyro frequency or anisotropic, slow-magnetosonic waves below the ion gyro frequency could be generated by electrically charged space objects for potential detection and tracking. Plasma simulations have been tested with laboratory experiments showing that both shear and compressional Alfvén wave solitons require a space object velocity compatible to or greater than the Alfvén speed in the plasma. Before the presentation of the results in this paper, no other efforts in space has been made to

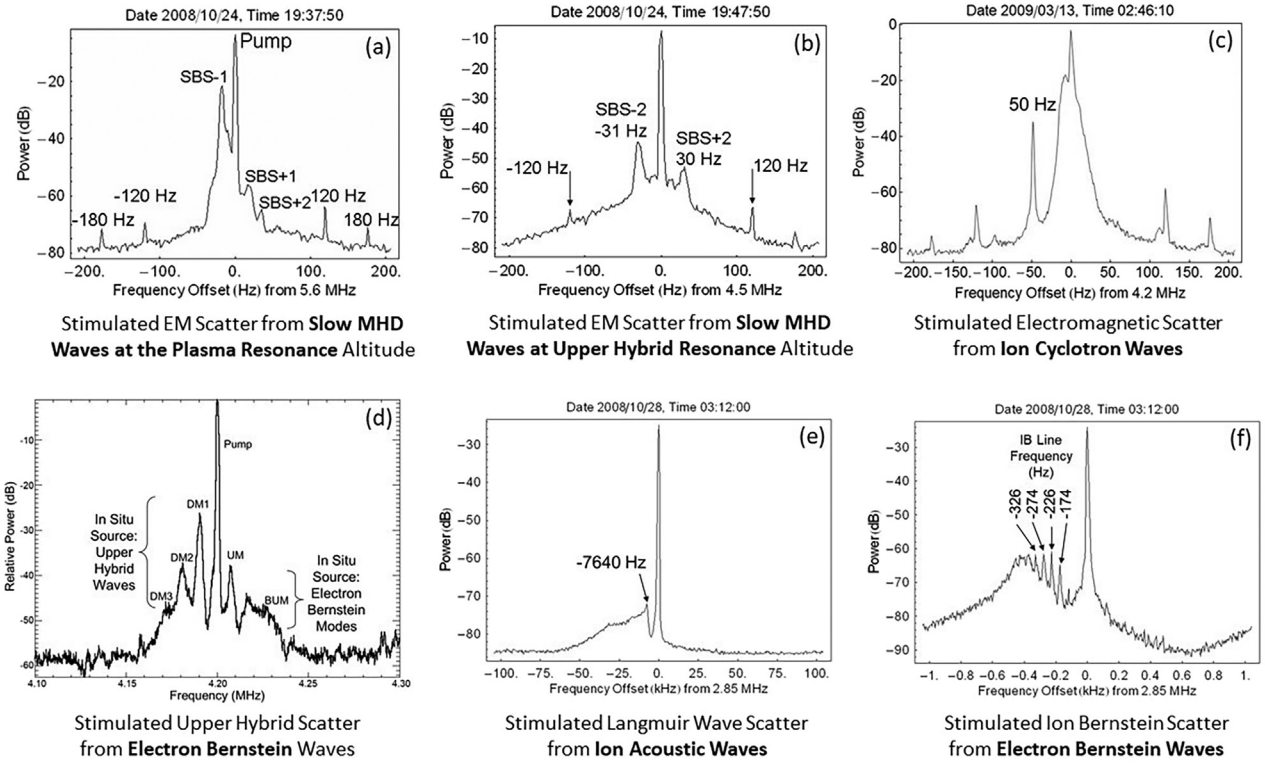

FIG. 22. Six examples of stimulated electromagnetic emissions from high power HF waves that generate parametric decay products such as slow magnetosonic waves (a) at the Langmuir wave reflection altitude and (b) upper hybrid resonance altitude, (c) ion cyclotron waves, (d) lower hybrid waves, (e) ion acoustic waves, and (d) and (f) electron and ion Bernstein waves.

measure what waves are actually produced by inert space objects moving through the ionosphere. The theory that space objects produce detectable ion acoustic solitons was not borne out by the observations but an alternative theory is proposed that the waves are compressional Alfvén waves produced by the Cherenkov process.

Extending this type of Cherenkov simulation to a 3D Cartesian geometry with compressional Alfvén waves and whistlers will be explored in future work. A detailed Cherenkov model is currently under development to determine if the compressional Alfvén waves, which are not constrained to magnetic field lines, will propagate a disturbance in all directions to account for 25 km or more observation ranges. The Cherenkov-like model can be extended to plasmas with multiple ion species, each species with a different mass.[64] which is essential for satellite motion in the plasmasphere composed of both O^+, H^+, He^+ ions. The results for the Cherenkov-like model will be tested to match the *in situ* observations of plasma waves measured with the Swarm-E electric field instrument as described earlier. Future research on models of plasma wave generation by orbital objects will consider (a) the effects of solar EUV ionizing radiation and (b) precipitating auroral electrons on low-altitude charging.

In this paper, theoretical concepts have been compared with the observations of (1) long range (200 to 400 km) soliton-like observations of transient driven, compressional-Alfvén waves from Space Shuttle OMS engine burns (Fig. 2) (2) local (self-observations) of spacecraft driven lower-hybrid or ion-acoustic waves recorded with the Swarm-E RRI sensor (Fig. 4), and (3) near field (1 to 50 km) observations of compressional Alfvén waves of target objects by the host RRI sensor (Figs. 7–13). Based on these experimental measurements, new theories have been proposed and are needed for generation of linear compressional-Alfvén waves which propagate nearly perpendicular to the ambient magnetic field and have a frequency range from below the ion cyclotron frequency and cutoff near the local lower hybrid frequency. Using the *in situ* observation technique, Swarm-E and other spacecraft hosting both electric and magnetic field sensors will continue provide data to both motivate and validate theory, simulations, laboratory, and future space systems designed for observation of space objects using plasma waves. Future models of MHD waves from space debris will be formulated with validation by the observations and predictions from space debris.

Finally, the spacecraft charging process must be considered for generation of plasma waves from objects in low earth orbit. It should be emphasized that all passive satellites are charged negative when orbiting at low earth orbit in the ionosphere. The models of nonlinear wave production by satellites incorrectly have used a positively charged space object need to be reexamined. With a steady state electric charge in orbit through a uniform background plasma, the pinned fluctuations, trailing potential reductions, transient wave disturbances and ram solitons will be produced as shown in Fig. 16 depend on the spatial and temporal distribution of source charges. The Gaussian and Lorentzian charge functions for the external currents in (5) and (6) were only chosen for ease of analytic computations. Actual charge distributions on a space object will depend on the object shape and orientation. Temporal fluctuations in the charge state of a space object, which are influenced by the charging environment,[81–83] could launch wake disturbances. The measurements of plasma waves from known spacecraft should be correlated with measurements in ionizing radiation and auroral precipitation[84,85] that can influence spacecraft charging.

ACKNOWLEDGMENTS

The authors thank Professor Christine Hartzell, Dr. Alexis Truitt, Dr. James Roeder, and Dr. Bengt Eliasson for helpful discussions. The work at the University of Alaska was supported by NSF under Grant No. 2054361 and by NASA under Grant No. 80NSSC23K0529. The European Space Agency's Third Party Mission Program supports the e-POP instruments on the CASSIOPE/Swarm-E satellite.

AUTHOR DECLARATIONS

Conflict of Interest

The authors have no conflicts to disclose.

Author Contributions

Paul A. Bernhardt: Conceptualization (equal); Formal analysis (equal); Funding acquisition (equal); Investigation (equal); Methodology (equal); Writing – original draft (equal); Writing – review & editing (equal). **Lauchie Scott:** Conceptualization (equal); Funding acquisition (equal); Investigation (equal); Writing – review & editing (equal). **Andrew Howarth:** Conceptualization (equal); Data curation (equal); Funding acquisition (equal); Investigation (equal); Writing – review & editing (equal). **George J. Morales:** Conceptualization (equal); Formal analysis (equal); Investigation (equal); Writing – review & editing (equal).

DATA AVAILABILITY

The data that support the findings of this study are openly available in e-POP Data Center, Ref. 86.

REFERENCES

[1]L. C. Lee and J. R. Kan, "Nonlinear ion-acoustic waves and solitons in a magnetized plasma," Phys. Fluids **24**, 430 (1981).
[2]I. Kulikov and M. Zak, "Detection of moving targets using soliton resonance effect," Adv. Remote Sens. **1**, 58–63 (2012).
[3]A. Sen, S. Tiwari, S. Mishra, and P. Kaw, "Nonlinear wave excitations by orbiting charged space debris objects," Adv. Space Res. **56**(3), 429–435 (2015).
[4]R. M. Albarran and A. Barjatya, "Plasma density analysis of CubeSat wakes in the Earth's ionosphere," J. Spacecr. Rockets **53**(3), 1–8 (2016).
[5]S. Jaiswal, S. P. Bandyopadhyay, and A. Sen, "Experimental observation of precursor solitons in a moving complex plasma," Phys. Rev. E **93**, 041201(R) (2016).
[6]S. K. Tiwari and A. Sen, "Wakes and precursor soliton excitations by a moving charged object in a plasma," Phys. Plasmas **23**, 22301 (2016).
[7]S. K. Tiwari and A. Sen, "Fore-wake excitations from moving charged objects in a complex plasma," Phys. Plasmas **23**, 100705 (2016).
[8]G. Arora, P. Bandyopadhyay, M. G. Hariprasad, and A. Sen, "Effect of size and shape of a moving charged object on the propagation characteristics of precursor solitons," Phys. Plasmas **26**, 93701 (2019).
[9]A. S. Truitt and C. M. Hartzell, "Simulating damped ion acoustic solitary waves from orbital debris," J. Spacecr. Rockets **57**, 975 (2020).
[10]A. S. Truitt and C. M. Hartzell, "Simulating plasma solitons from orbital debris using the forced Korteweg–de Vries equation," J. Spacecr. Rockets **57**, 876 (2020).
[11]S. P. Acharya, A. Mukherjee, and M. S. Janaki, "Accelerated magnetosonic lump wave solutions by orbiting charged space debris," Nonlinear Dyn. **105**, 671 (2021).
[12]A. Mukherjee, S. P. Acharya, and M. S. Janaki, "Dynamical study of nonlinear ion acoustic waves in presence of charged space debris at Low Earth Orbital (LEO) plasma region," Astrophys. Space Sci. **366**, 7 (2021).

[13]A. S. Truitt and C. M. Hartzell, "Three-dimensional KP damped forced ion acoustic solitary waves from orbital debris," J. Spacecr. Rockets **58**, 848 (2021).
[14]S. P. Acharya, A. Mukherjee, and M. S. Janaki, "Charged space debris induced nonlinear magnetosonic waves using inertial magnetohydrodynamics," Adv. Space Res. **69**, 4045 (2022).
[15]I. M. DesJardin and C. M. Hartzell, "Nonlinear spectral analysis of ion acoustic solitons arising from a streaming charged object using the numerical inverse scattering transform," Phys. Plasmas **29**, 112116 (2022).
[16]A. Sen, R. Mukherjee, S. K. Yadav, C. Crabtree, and G. Ganguli, "Electromagnetic pinned solitons for space debris detection," Phys. Plasmas **30**, 012301 (2023).
[17]D. Wright, "Colliding satellites: Consequences and implications," in *Union Concerned Scientists* (Citizens and Scientist for Environmental Solutions, 2009).
[18]A. Aghabarati, R. Moini, S. Ladan, S. Fortin, and F. P. Dawalibi, "Electromagnetic shielding properties of spherical polyhedral structures generated by conducting wires and metallic surfaces," in *IEEE International Symposium on Electromagnetic Compatibility (EMC)* (IEEE, 2016), pp. 277–282.
[19]J. D. Huba and H.-L. Liu, "Global modeling of equatorial spread *F* with SAMI3/WACCM-X," Geophys. Res. Lett. **47**, e2020GL088258, https://doi.org/10.1029/2020GL088258 (2020).
[20]D. R. Nicholson, *Introduction to Plasma Theory* (John Wiley & Sons, New York, 1983), pp. 177–185.
[21]T. H. Stix, *Waves in Plasmas* (Springer-Verlag, 1992).
[22]D. G. Swanson, *Plasma Waves* (Academic Press, Inc., Boston, 1989), Vol. 267–269, pp. 173–175.
[23]P. A. Bernhardt, J. O. Ballenthin, J. L. Baumgardner, A. Bhatt, I. D. Boyd, J. M. Burt, A. Coster, P. J. Erickson, J. D. Huba, G. D. Earle, C. R. Kaplan, J. C. Foster, K. M. Groves, R. A. Haaser, R. A. Heelis, D. E. Hunton, D. L. Hysell, J. H. Klenzing, M. F. Larsen, F. D. Lind, T. R. Pedersen, R. A. Stoneback, P. A. Roddy, S. P. Rodriquez, G. S. San Antonio, P. W. Schuck, C. L. Siefring, C. A. Selcher, S. M. Smith, E. R. Talaat, J. F. Thomason, R. T. Tsunoda, and R. H. Varney, "Ground and space-based measurement of rocket engine burns in the ionosphere," IEEE Trans. Plasma Sci. **40**, 1267–1286 (2012).
[24]A. R. Soto, C. Crabtree, G. Ganguli, and A. C. Fletcher, "Lower-hybrid wave instability due to multiple fast heavy ion ring distributions in the SMART experiment," Phys. Plasmas **27**, 122112 (2020).
[25]D. Winske and W. Daughton, "Generation of lower hybrid and whistler waves by an ion velocity ring distribution," Phys. Plasmas **19**, 072109 (2012).
[26]M. Lesur, P. H. Diamond, and Y. Kosuga, "Nonlinear current-driven ion-acoustic instability driven by phase-space structures," Plasma Phys. Controlled Fusion **56**, 075005 (2014).
[27]M. Mithaiwala, L. Rudakov, and G. Ganguli, "Stability of an ion-ring distribution in a multi-ion component plasma," Phys. Plasmas **17**, 042113 (2010).
[28]See https://epop.phys.ucalgary.ca/payload/ for the descriptions of the eight science payloads on Swarm-E.
[29]P. A. Bernhardt, M. K. Griffin, W. C. Bougas, A. D. Howarth, H. G. James, C. L. Siefring, and S. J. Briczinski, "Satellite observations of strong plasma wave emissions with frequency shifts induced by an engine burn from the Cygnus spacecraft," Radio Sci. **56**, e2020RS007143, https://doi.org/10.1029/2020RS007143 (2020).
[30]G. T. Ruck and D. E. Barrick, *Radar Cross Section Handbook* (Plenum Press, New York, 1970), Vol. 1 & 2.
[31]D. B. Graham, Y. V. Khotyaintsev, C. Norgren, A. Vaivads, M. André, J. F. Drake, J. Egedal, M. Zhou, O. L. Contel, J. M. Webster, B. Lavraud, I. Kacem, V. Génot, C. Jacquey, A. C. Rager, D. J. Gershman, J. L. Burch, and R. E. Ergun, "Universality of lower hybrid waves at Earth's magnetopause," J. Geophys. Res.: Space Phys. **124**, 8727, https://doi.org/10.1029/2019JA027155 (2019).
[32]P. A. Bernhardt, R. A. Roussel-Dupre, M. B. Pongratz, G. Haerendel, A. Valenzuela, D. A. Gurnett, and R. R. Anderson, "Observations and theory of the AMPTE magnetotail barium releases," J. Geophys. Res. **92**(A6), 5777–5794, https://doi.org/10.1029/JA092iA06p05777 (1987).
[33]L. Wei *et.al.*, "Generation of the fluctuations by a charged dust beam in the ionosphere," J. Plasma Phys. **88**(1), 905880118 (2022).
[34]M. Andre, E. Odelstad, D. B. Graham, A. I. Eriksson, T. Karlsson, G. Stenberg Wieser, E. Vigren, C. Norgren, F. L. Johansson, P. Henri, M. Rubin, and I. Richter, "Lower hybrid waves at comet 67P/Churyumov–Gerasimenko," Mon. Not. R. Astron. Soc. **469**, S29–S38 (2017).
[35]P. A. Bernhardt, W. C. Bougas, M. K. Griffin, C. Watson, R. B. Langley, A. D. Howarth, H. G. James, C. L. Siefring, G. W. Perry, J. D. Huba, R. C. Moore, M. B. Cohen, and M. Gołkowski, "Strong amplification of ELF/VLF signals in space using neutral gas injections from a satellite rocket engine," Radio Sci. **56**, e2020RS007207, https://doi.org/10.1029/2020RS007207 (2020).
[36]R. C. Davidson and N. T. Gladd, "Anomalous transport properties associated with the lower-hybrid-drift instability," Phys. Fluids **18**, 1327 (1975).
[37]D. B. Graham, Y. V. Khotyaintsev, C. Norgren, A. Vaivads, M. Andre, S. Toledo-Redondo, and J. L. Burch, "Lower hybrid waves in the ion diffusion and magnetospheric inflow regions," J. Geophys. Res.: Space Phys. **122**(1), 517–533, https://doi.org/10.1002/2016JA023572 (2017).
[38]H. Romero, G. Ganguli, and Y. C. Lee, "Ion acceleration and coherent structures generated by lower hybrid shear-driven instabilities," Phys. Rev. Lett. **69**(24), 3503 (1992).
[39]E. Odelstad, T. Karlsson, A. Eriksson, S. Bergman, and G. Stenberg Wieser, "Ion-ion cross-field instability of lower hybrid waves in the inner coma of comet 67P," J. Geophys. Res.: Space Phys. **127**, e2022JA030535, https://doi.org/10.1029/2022JA030535 (2022).
[40]T. E. Stringer, "Low-frequency waves in an unbounded plasma," J. Nucl. Energy, Part C **5**, 89 (1963).
[41]K. S. Yeh and C. H. Liu, *Theory of Ionospheric Waves* (Academic Press, New York, 1972).
[42]D. A. Tidman and N. A. Krall, *Shock Waves in Collisionless Plasmas* (Wiley, New York, 1971).
[43]T. Cattaert, "Large amplitude solitary waves in space plasmas," Ph.D. thesis (Gent University, 2006).
[44]T. Cattaert and F. Verheest, "Large amplitude parallel propagating electromagnetic oscillations," Phys. Plasmas **12**, 012307 (2005).
[45]R. C. Davidson, *Methods in Nonlinear Plasma Theory* (Elsevier, 1972).
[46]W. Horton and Y.-H. Ichikawa, *Chaos and Structures in Nonlinear Plasmas* (Word Scientific, 1996).
[47]A. Kumar, C. Shukla, D. Verma, A. Das, and P. Kaw, "Excitation of KdV magnetosonic solitons in plasma in the presence of an external magnetic field," Plasma Phys. Controlled Fusion **61**, 065009 (2019).
[48]A. Kumar and A. Sen, "Precursor magnetosonic solitons in a plasma from a moving charge bunch," New J. Phys. **22**, 073057 (2020).
[49]R. Z. Sagdeev, "Cooperative phenomena and shock waves in collisionless plasmas," Rev. Plasma Phys. **4**, 23 (1966).
[50]M. Y. Yu and P. K. Shukla, "Finite amplitude solitary Alfvén waves," Phys. Fluids **21**, 1457 (1978).
[51]E. Ott and R. N. Sudan, "Nonlinear theory of ion acoustic waves with Landau damping," Phys. Fluids **12**, 2388 (1969).
[52]S. Clarke, K. Gorshkov, R. Grimshaw, and T. Stepanyants, "Decay of Kadomtsev–Petviashvili lumps in dissipative media," Physica D **366**, 43–50 (2018).
[53]M. S. Ruderman, "Kadomtsev-Petviashvili equation for magnetosonic waves in Hall plasmas and soliton stability," Phys. Scr. **95**, 095601 (2020).
[54]L. M. Duncan, J. Sheerin, and R. Behnke, "Observations of ionospheric cavities generated by high-power radio waves," Phys. Rev. Lett. **61**(2), 239–242 (1988).
[55]A. V. Gurevich, H. C. Carlson, Y. V. Medvedev, and K. P. Zybin, "Langmuir turbulence in ionospheric plasma," Plasma Phys. Rep. **30**(12), 995–1005 (2004).
[56]M. T. Rietveld, A. Senior, J. Markkanen, and A. Westman, "New capabilities of the upgraded EISCAT highpower HF facility," Radio Sci. **51**, 1533–1546, https://doi.org/10.1002/2016RS006093 (2016).
[57]K. Nishikawa, "Parametric excitation of coupled waves. II. Parametric plasmon-photon interaction," J. Phys. Soc. Jpn. **24**, 1152–1158 (1968).
[58]P. A. Bernhardt, C. A. Tepley, and L. M. Duncan, "Airglow enhancements associated with plasma cavities formed during ionospheric heating experiments," J. Geophys. Res. **94**, 9071–9092, https://doi.org/10.1029/JA094iA07p09071 (1989).
[59]P. A. Bernhardt, W. A. Scales, S. M. Grach, A. N. Karashtin, D. S. Kotik, and S. V. Polyakov, "Excitation of artificial airglow by high power radio waves from the 'SURA' Ionospheric Heating Facility," Geophys. Res. Lett. **18**, 1477–1480, https://doi.org/10.1029/91GL01847 (1991).

[60]P. A. Bernhardt, M. Wong, J. D. Huba, B. G. Fejer, L. S. Wagner, J. A. Goldstein, C. A. Selcher, V. L. Frolov, and E. N. Sergeev, "Optical remote sensing of the thermosphere with heater induced artificial airglow (HIAA)," J. Geophys. Res. **105**, 10657–10671, https://doi.org/10.1029/1999JA000366 (2000).
[61]P. A. Bernhardt, N. A. Gondarenko, P. N. Guzdar, F. T. Djuth, C. A. Tepley, M. P. Sulzer, S. L. Ossakow, and D. L. Newman, "Using radio-induced aurora to measure the horizontal structure of ion layers in the lower thermosphere," J. Geophys. Res. **108**(A9), 1336, https://doi.org/10.1029/2002JA009712 (2003).
[62]A. S. Leonovich and D. A. Kozlov, "Magnetosonic resonances in the magnetospheric plasma," Earth Planet Space **65**, 369–384 (2013).
[63]B. Van Compernolle, G. J. Morales, and W. Gekelman, "Cherenkov radiation of shear Alfvén waves," Phys. Plasmas **15**, 082101 (2008).
[64]W. A. Farmer and G. J. Morales, "Cherenkov radiation of shear Alfvén waves in plasmas with two ion species," Phys. Plasmas **19**, 092109 (2012).
[65]L. Mandi, A. Saha, and P. Chatterjee, "Dynamics of ion-acoustic waves in Thomas-Fermi plasmas with source term," Adv. Space Res. **64**, 427–435 (2019).
[66]G. J. Morales, R. S. Loritsch, and J. E. Maggs, "Structure of Alfvén waves at the skindepth scale," Phys. Plasmas **1**, 3765 (1994).
[67]M. R. Oberhardt, D. A. Hardy, D. C. Thompson, W. J. Raitt, E. Melchioni, C. Bonifazi, and M. P. Gough, "Positive spacecraft charging as measured by the shuttle potential and return electron experiment," IEEE Trans. Nucl. Sci. **40**(6), 1532–1541 (1993).
[68]S. T. Lai, *Fundamentals of Spacecraft Charging* (Princeton University Press, Princeton, New Jersey, 2012).
[69]J. L. Roeder and V. K. Jordanova, "Space weather effects and prediction," in *Ring Current Investigations: The Quest for Space Weather Prediction*, edited by V. K. Jordanova, R. Ilie, and M. Chen (Elsevier, 2020), Chap. 8.
[70]P. A. Bernhardt and M. P. Sulzer, "Incoherent scatter measurements of ion beam disturbances produced by space shuttle exhaust injections into the ionosphere," J. Geophys. Res. **109**, A02303, https://doi.org/10.2514/6.2001-4705 (2004).
[71]G. Tóth, Y. Chen, T. I. Gombosi, P. Cassak, S. Markidis, and I. B. Peng, "Scaling the ion inertial length and its implications for modeling reconnection in global simulations," J. Geophys. Res.: Space Phys. **122**, 10,336–10,355, https://doi.org/10.1002/2017JA024189 (2017).
[72]D. R. Shklyar, M. Parrot, J. Chum, O. Santolik, and E. E. Titova, "On the origin of lower- and upper-frequency cutoffs on wedge/like spectrograms observed by DEMETER in the midlatitude ionosphere," J. Geophys. Res. **115**, A05203, https://doi.org/10.1029/2009JA014672 (2010).
[73]J. D. Jackson, *Classical Electrodynamics* (Wiley, 1975), Chap. 13.
[74]J. Cubas, A. Farrahi, and S. Pindado, "Magnetic attitude control for satellites in polar or sun-synchronous orbits," J. Guid., Control, Dyn. **38**, 1947–1958 (2015).
[75]K. Kondo, I. Kolmanovsky, Y. Yoshimura, M. Bando, S. Nagasaki, and T. Hanada, "Nonlinear model predictive detumbling of small satellites with a single-axis magnetorquer," J. Guid., Control, Dyn. **44**(4), 1–8 (2021).
[76]A. C. Nicholas, C. R. Englert, C. M. Brown, T. T. Finne, K. D. Marr, C. R. Binz, L. M. Healy, and S. T. Kindl, "Lightsheet sensor for the detection of orbital debris," in First International Orbital Debris Conference, 2019.
[77]P. A. Bernhardt, C. L. Siefring, S. J. Briczinski, M. McCarrick, and R. G. Michell, "Large ionospheric disturbances produced by the HAARP HF facility," Radio Sci. **51**, 1081–1093, https://doi.org/10.1002/2015RS005883 (2016).
[78]P. A. Bernhardt, C. A. Selcher, R. H. Lehmberg, S. P. Rodriguez, J. F. Thomason, K. M. Groves, M. J. McCarrick, and G. J. Frazer, "Stimulated Brillouin scatter in a magnetized ionospheric plasma," Phys. Rev. Lett. **104**, 165004 (2010).
[79]P. A. Bernhardt, C. A. Selcher, and S. Kowtha, "Electron and ion Bernstein waves excited in the ionosphere by high power EM waves at the second harmonic of the electron cyclotron frequency," Geophys. Res. Lett. **38**, L19107, https://doi.org/10.1029/2011GL049390 (2011).
[80]B. Eliasson, A. Senior, M. Rietveld, A. D. R. Phelps, R. A. Cairns, K. Ronald, D. C. Speirs, R. M. G. M. Trines, I. McCrea, R. Bamford, J. T. Mendonça, and R. Bingham, "Controlled beat-wave Brillouin scattering in the ionosphere," Nat. Commun. **12**, 6209 (2021).
[81]J. R. Dennison, R. C. Hoffmann, and J. Abbott, "Triggering Threshold Spacecraft Charging with Changes in Electron Emission from Materials," AIAA Paper No. 2007-1098, 2007.
[82]J. F. Fennell, H. C. Koons, J. L. Roeder, and J. B. Blake, "Spacecraft charging. Observations and relationship to satellite anomalies," Report No. TR-2001 (8570)-5, 2001.
[83]J.-C. Matéo-Vélez, A. Sicard, D. Payan, N. Ganushkina, N. P. Meredith, and I. Sillanpäa, "Spacecraft surface charging induced by severe environments at geosynchronous orbit," Space Weather **16**, 89–106, https://doi.org/10.1002/2017SW001689 (2018).
[84]P. C. Anderson, "Characteristics of spacecraft charging in low Earth orbit," J. Geophys. Res. **117**, A07308, https://doi.org/10.1029/2011JA016875 (2012).
[85]N. Ahmad, H. Usui, and Y. Miyake, "Particle in cell simulation to study the charging and evolution of wake structure of LEO spacecraft," in *Methods and Applications for Modeling and Simulation of Complex Systems. AsiaSim 2018. Communications in Computer and Information Science*, edited by L. Li, K. Hasegawa, and S. Tanaka (Springer, Singapore, 2018), Vol 946.
[86]HTTP access to Swarm-E data via a date-driven folder tree. Allows for quick look and summary file browsing. No login required; see https://epop-data.phys.ucalgary.ca/